HYDROTHERMAL ORGANIC AGGREGATES ASSOCIATED WITH THE HIGH-NI GRADES OF THE CERRO MATOSO LATERITE DEPOSIT, MONTELÍBANO, COLOMBIA

Andrés Castrillón✉, **Thomas Heinrich Cramer** and **Javier Guerrero**

Departamento de Geociencias, Universidad Nacional de Colombia, Bogotá, Colombia.
✉ *Corresponding author, e-mail: acastrillonp@unal.edu.co*

Keywords: *Hydrothermal systems; black mudstones; nickel laterite; peridotites; green saprolite; Cerro Matoso; Colombia.*

ABSTRACT

Mineralogical and geochemical analyses (EDS, ICP-MS, XRD) of black mudstones locally overlying the peridotites of Cerro Matoso at Pit-1 link these sediments with deep-sea hydrothermal systems. In this unit, rounded particles were identified that would correspond with organic aggregates commonly found in reducing environments related to hydrothermal vent systems. These aggregates are formed by methane-producing microorganism (methanogens) metabolism that sustains such extreme environments mediated by anaerobic methane-consuming cell consortia. The organic aggregates register Ni content up to 8 wt%. For this fossilized methanogen-AOM (Anaerobic Oxidation of Methane) consortium we propose an ultramafic contribution, followed by a hydrothermal enrichment of Black/White-Smoker type and a supplementary contribution of bio-mineralized Ni of the organics within the sediments during the formation of the Ni-bearing deposit. The sediments configured an atypical lateritic profile at the Pit-1 where Ni-concentrations reached up to 8 wt%, in contrast to the southern Pit-2 where the peridotites developed a typical lateritic profile with nickel concentrations not exceeding 4 wt%. During the Cretaceous and Cenozoic, the ultramafic rocks and associated deep-sea hydrothermal-related sediments were accreted to the South American continent. They were recently exhumed allowing supergene Ni-enrichment forming the laterite deposit known today with its locally extraordinary high Ni contents. Together with the organics, authigenic phyllosilicates and Fe-(oxy) hydroxides are the main ‘‘ore minerals” that contributed to add the lateritic Ni-enrichment after supergene leaching processes due to weathering of the Cerro Matoso peridotites.

INTRODUCTION

The only economically mineable nickel deposit known so far in Colombia is located 100 km southeast of Monteria in the Department of Córdoba. The mining complex of Cerro Matoso has an annual production of approximately 41.1kt of ferronickel, 32 Mt total reserves with a pondered average of 1.2 wt% Ni and thus a static life of 10 years (South32, 2019), although the measured + indicated + inferred laterite resources sum 312 Mt @ 0.9% Ni, + stockpiles of 43 Mt @ 1.2 wt% Ni. In this Australian South32-owned complex, the nickel ore is mined, molten, and processed to produce, in one of the largest lateritic nickel mines worldwide, an alloy of iron and nickel of high purity and low carbon content, for exportation to the international markets, mainly Asia. Recently, the company South32 began extraction of laterites from the Queresas and Porvenir hills, located 30 km north of Cerro Matoso deposit in the Planeta Rica peridotites. The only available report so far for the Planeta Rica deposit is from the United Nations, published in 1975. This report calculated Ni reserves of 5.2 Mt on a dry basis. Berger et al. (2011) resumed that laterites contain about 70 percent of world nickel resources that have been mined for more than 100 years, and account for about 40 percent of world nickel production.

Using XRD, BSE-EDX and SEM analyses Castrillón (2019), described petrographic and mineralogical characteristics of mudstones overlying the Cerro Matoso peridotites in the Pit-1, remarking that this new Fe-Ni-ore unit corresponds to deep marine sediments that can be separated in two units, identified as black mudstone facies I and facies II. The facies I is composed of berthierine + greenalite (55 vol%), siderite (38 vol%), and goethite (7 vol%) while the facies II includes greenalite (10 to 40 vol%), siderite (30-70 vol%), chromite (< 3 vol%), and magnetite (14 vol%). These rocks represent sediments which may be ancient analogues of the modern metalliferous sediments and oxy-hydroxides in spreading ridge areas with volcanic activity.

The formation of deep-sea Fe-rich sediments that overlie oceanic crust has been well documented in the Pacific Ocean. According to Hein et al. (1997) and Kuhn et al. (1998), these deposits consist of of Fe-Mn oxyhydroxides and clay minerals that are efficient scavengers for trace elements such as Ni, Co, Cu and Rare Earth Elements (REE). Metalliferous sediments derived from a complex mixture of a vent plume fall-out, sulfide mound debris, and biogenic sedimentation processes (Boström and Peterson, 1969; Metz et al., 1988; German et al., 1993; Mills et al., 1993), which are dominated by polymetallic sulfide crystallization and Fe oxidation and by precipitation of plumes when hot reduced hydrothermal fluids are mixed with cold-oxygenated deep-sea water (Feely et al., 1987).

Marine currents disperse the fine-grained particulates derived from hydrothermal venting until they eventually settle out to form metal-enriched sediments beneath the overlying plume (Baker et al., 1985). Plume vent particles from deep-sea sediments may be related to organic processes that according to Toner et al. (2009) participated in the Fe cycling in deep-sea hydrothermal plumes. Additionally, they are related to the high nickel grades in the laterite deposit of Cerro Matoso, specifically at Pit-1, with Ni grades exceeding 8-9 wt% where black Fe-rich mudstones overlie the peridotites. Although little is known about the processes or dynamics of the plume environment, some particles have been described as bio-mineralization products (e.g., Konhauser et al., 2002; Kappler et al., 2005; Konhauser and Riding, 2012).

Microorganism consortia participate in the bio-mineralization by (AOM), a process that frequently is coupled to sulfate reduction and usually accompanied by methanogens,

a group of strict anaerobic micro-organisms, that produce methane and are phylogenetically affiliated to the kingdom Euarchaeota of the domain Archaea (Woese et al., 1990). This latter can be active just below 110ºC (Kotelnikova, 2002). Thes reaction is mediated by the association between anaerobic methanotrophic Archaea (ANME) and sulfate-reducing bacteria (SRB) (Chen et al., 2014). These microbial organisms are widely distributed, from marine hydrothermal vents, deep biosphere, cold seep systems, sulfate-methane transition zone of sediments, and marine water columns, but also in terrestrial habitats such as mud volcanoes, landfills, and the anoxic portions of freshwater lakes (Boetius et al., 2000; Grossman et al., 2002; Alain et al., 2006; Knittel and Boetius, 2009). At some vents it is not uncommon for hosts thiotrophs and methanotrophs to live side by side, and, in some cases, bacteria capable of methanotrophy and thiotrophy can be found in the same host (Tyler and Young, 2003). According to Gadd (2010), the organic matrix of AOM consortia may facilitate the nucleation of minerals. However, the composition and the mechanism of mineralization on the exopolymers of the AOM of such consortia are poorly understood (Kotelnikova, 2002; Chen et al., 2014).

The AOM consortia (i.e., ANME-2 and SRB) are spherical with diameters of around 3-20 μm, and have two different spatial arrangements of cells, shell-type, and mixed-type. Shell-type consortia have a well-known morphology with an inner core of ANME, which is partially or fully surrounded by outer SRB, whereas the ANME and SRB of the mixed-type are completely mixed to form irregular shapes usually enclosed by a thick organic matrix (i.e., those containing ANME-2) (Nauhaus et al., 2007; Knittel and Boetius, 2009; Chen et al., 2014). This nearly invisible microbial life is responsible for the majority of the chemical cycling that occurs in these habitats, offering essential ecosystem services for deep-sea environments (Orcutt et al., 2018). Despite the importance of the microscopic component of life to ecosystem services in the deep sea, these microorganisms have been largely overlooked. According to Campbell (2006), stable isotopes of carbon and oxygen in vent-seep-carbonates are biogeochemical archives of past fluid activity and composition that can show fine-scale isotopic change throughout their growth and development. Han et al. (2004) suggest that isotopically depleted carbonate-carbon signals recorded in some seep deposits are derived from microbially mediated AOM that occurs in the sulfate reduction zone. In general terms, after organic matter microbial degradation, HCO_3^- preserves the same isotopic signal as the source organic material, e.g. characterized by $\delta^{13}C$ values between -20‰ and -25‰ for marine environments (Whiticar, 1999). In the case of ultramafic-hosted hydrothermal systems $\delta^{13}C$ values of CH_4 from mantle fluids would be preserved.

Carbon stable isotopes have been used to determine the source and dynamic of CO_2 in ultramafic-hosted systems, such as the Lost City, Rainbow, and Logatchev vent fields, as well as the sediments and fauna hosted in these environments (Hentscher, 2012). The $\delta^{13}C_{PDB}$ values of CH_4 from these systems are heavy (Lost City -14 to -9‰, Rainbow -16‰, Logatchev -14‰) in contrast to isotopic light values of thermogenic CH_4 (-50 to -30‰) (Sherwood et al., 2006). Similar analysis has been used to characterize chemosynthetic fossil assemblages found in these environments (e.g., Eickmann et al., 2009 a,b; Lartaud et al., 2010). In general, methane from serpentinizing environments tends to be enriched in ^{13}C compared to locations where it is derived predominantly from biological methanogenesis or the thermogenic degradation of organic matter (Schrenk et al., 2013). According to Furnes et al. (2001), the CO_2 bioproduction is compatible with microbe-induced fractionation during oxidation of organic matter and is reflected in the negative $\delta^{13}C$ values of calcite extracted from in situ oceanic crust.

Here, we use petrographic and BSE/EDS electron microscopy (SEM), ICP-MS analyses, and pyrolysis analyses for TOC, to investigate the microscopic particles and clay fraction found in the black mudstone succession overlying the peridotites from the Cerro Matoso deposit. The main goal of this research is to provide new evidences that support the hydrothermal origin of the sediments where organic aggregates are one of the main Ni supply that enrich the laterite profile formed by the ultramafic rocks. This scenario makes the Cerro Matoso very different from usual Ni-laterites deposits.

GEOLOGICAL SETTING

Most known ultramafic bodies in Central and northern South America are associated with the Caribbean Plate margin (e.g., López-Rendón, 1986, Lewis et al., 2006). Tectonic processes exhumed and exposed Ni-bearing peridotites to intense humid tropical weathering forming laterite profiles resulting in secondary nickel enrichment (Banerji, 1982; Friedrich et al., 1987; Bardossy, 1989; Bardossy and Aleva, 1990; Schwarz, 1994; Gleeson et al., 2004; Lewis et al., 2006). Some of these lateritic nickel deposits are mined, e.g. in the central part of the Dominican Republic (Loma Caribe), eastern Cuba (Mayari, Nicaro Moa Bay, Punta Gorda), northern Venezuela (Loma de Níquel), and northwestern Colombia in Cerro Matoso (Fig. 1).

Ultramafic rocks may form domes associated to transform faults perpendicular to oceanic spreading ridges, where the detachment fault arrays produced thereby drag lower crustal magmatic chambers and triggered the emplacement of shallow-depth gabbro intrusions (Cann et al., 1997; Escartin et al., 2003; Cannat et al., 2006; Smith et al., 2006). This creates favorable conditions for the hydrothermal circulation systems in the serpentinite slab brought to the seafloor surface (Silantyev et al., 2009).

Ildefonse et al. (2007) proposed that the breaking-up of the oceanic plates in heterogeneous crust fragments does not produce vertical planes, but instead deep and slightly inclined faults appear to control most of the slow movement of the plate, thus exhuming and exposing lower crust and mantle rocks. Some of these rocks are exposed as oceanic core complexes (OCC), which are deep sections of the oceanic lithosphere exhumed to the seafloor by long-lived detachment faults formed along with slow and ultra-slow spreading centers at different scales (Cann et al., 1997; Escartin et al., 2003; Cannat et al., 2006; Smith et al., 2006). The OCC are formed perpendicular to the ridges near the end of the slow deployment segments although their evolution could suggest that fracture zones do not become locked immediately on transform-to-fracture transition (Cannat et al., 2006).

The domes can exceed 100 m of relief-high, several hundred meters in width and up to kilometers in length (Ildefonse et al., 2007), conditions that could be compared with the Cerro Matoso peridotites body.

The oceanic crust that builds today the Central Caribbean region was formed during the Cretaceous, about 89 Ma ago (Sinton et al., 1998)C. W., R. . Duncan, M. Storey, J. Lewis, and J. . Estrada, 1998, An oceanic flood basalt province within the Caribbean plate: Earth Planet Science Letter, v.

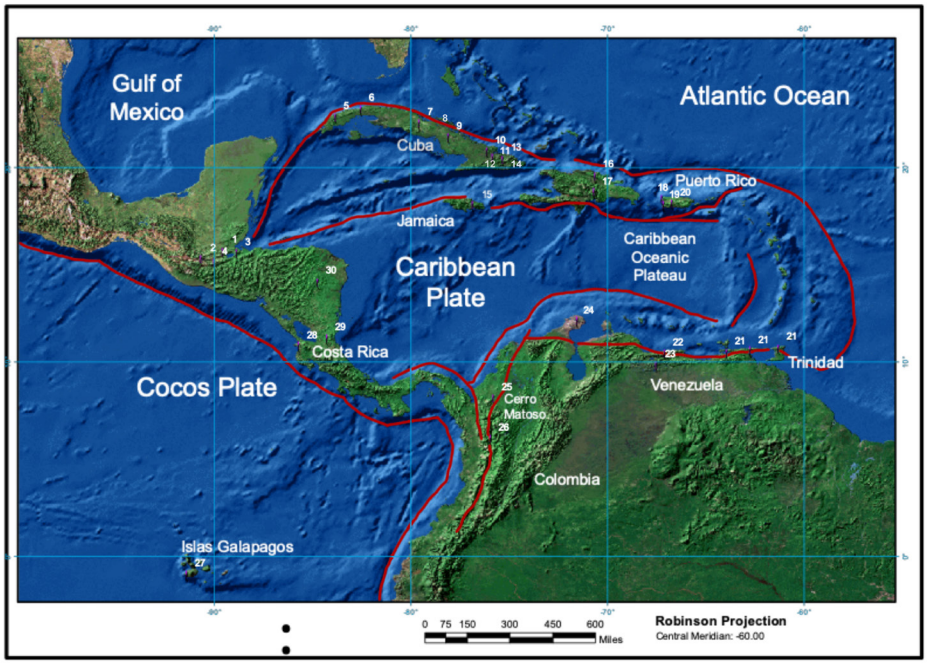

Fig. 1 - Ultramafic rock distribution in the Caribbean. 1: Sierra de Santa Cruz; 2: Baja Verapaz; 3: Juan de Paz; 4: Tambor Group (S and N Motagua), 5: Cajalbana; 6: Habana-Matanza: 7: Villa Clara; 8: Escambray; 9: Camaguey, 10: Holguin, 11: Mayari-Cristal; 12: Alto de la Corea, 13: Moa-Baracoa; 14: Sierra del Convento, 15: Arntully; 16: Costa Norte Belt; 17: Loma Caribe 18: Monte del Estado, 19: Rio Guanajibo; 20: Bermeja; 21: Franja Costera, 22: Loma de Niquel; 23: Villa de Cura; 24: La Guajira Peninsula (Cabo de la Vela Serpentinites); 25: Cerro Matoso, 26: Medellin Dunite, 27: Galapagos Islands, 28: Santa Elena, 29: Rio San Juan, 30: Siuna. Modified from Lewis et al. (2006).

155, p. 221\u2013235. The thick oceanic crust of the Caribbean plate appears to be the tectonized remnant of an eastern Pacific oceanic plateau that has been inserted between North and South America. The emplacement of the plateau into its present position has resulted in the obduction and exposure of its margins, providing an opportunity to study the age relations, internal structure and compositional features of the plateau. We present the results of 40Ar-39Ar radiometric dating, major-, trace-element, and isotopic compositions of basalts from some of the exposed sections as well as drill core basalt samples from Leg 15 of the Deep Sea Drilling Project. Five widely spaced, margin sections yielded ages ranging from 91 to 88 Ma. Less well-constrained radiometric ages from the drill cores, combined with the biostratigraphic age of surrounding sediments indicate a minimum crystallization age of ~90 Ma in the Venezuelan Basin. The synchroneity of ages across the region is consistent with a flood basalt origin for the bulk of the Caribbean plateau (i.e., large volume, rapidly erupted, regionally extensive volcanism in the Pacific Ocean, far west of its present position (Pindell and Barrett 1990; Pindell and Kennan 2009). As the American continent was moving to the west during the Late Cretaceous and the oceanic plate in turn was moving eastwards, oceanic segments were accreted in the western part of the continent (Lewis et al., 2006). Aspects of the collision and subduction or accretion in which the geometry of the process prevents an ophiolite segment from entering the subduction zone and instead preserves it against continental crust at shallow levels were discussed by Lewis et al. (2006). Accretion processes of ophiolitic segments in western Colombia were influenced by complex geometries at the time of the collision between the Caribbean-, Nazca-, Cocos- and South American Plates.

In the southern Caribbean, oblique convergence also resulted in the accretion of peridotites with high-pressure associations that may have started from the Eocene (55-50 Ma) and completed in the Oligocene or even in the early Miocene (30-15 Ma ago) (Lewis et al., 2006). These high-pressure associations appear to be the ones referred by Nívia (1997) as bodies accreted to the western edge of the South American Plate during the Eocene.

Relatively small bodies of serpentinized ultramafic rocks cropping out along the Caribbean mountain system in the northern coastal region of South America are associated with the southern margin of the Caribbean Plate. Associated with Paleozoic mafic gneisses and schists (Bellizia and Dengo, 1990), the Sierra Nevada de Santa Marta serpentinites crop out as a narrow and warped band at the north of Sevilla Fault (Chicangana et al., 2011). Associated with gabbroic lenses with dikes of basaltic andesites (Cardona et al., 2007) but also with Mesozoic and Early Cenozoic pelitic schists, phyllites, and marbles (Sepúlveda et al., 2003) the Cabo de la Vela serpentinites crop out at the Guajira Peninsula.

On the other hand, associations of Cretaceous mafic and ultramafic bands occur in north-south oriented belts in the Central and Western Cordilleras. Most of these bodies form thin elongated slabs of serpentinites associated with faults. Examples include Ituango, Heliconia, and Angelópolis serpentinites in the Antioquia Department, and the Philadelphia Serpentinites in the Caldas Department. Álvarez (1983) documented 28 occurrences of mafic-ultramafic bodies in the Western and Central Cordilleras of Colombia.

LOCAL GEOLOGY

The Cerro Matoso laterite deposit is an isolated body of peridotites (López-Rendón, 1986) located southeast of Montería in the province of Córdoba in northwest Colombia. Cerro Matoso is located to the west of the Romeral Fault System that coincides with a major boundary between oceanic crust on the west and continental crust on the east, although the name and the exact location are debated (e.g., Meissener et al., 1982; Cediel et al., 2003, Villagómez, 2010; Mora et al., 2017b) (Fig. 2a). The fault system is about 500 km long and marks the boundary between the accreted ophiolitic segments of the Western Cordillera and the poly-metamorphic continental core of the Central Cordillera. The origin of these ultramafic rocks may be associated with different oceanic fragments originated frommid-ocean ridge setting (e.g., Bartok et al., 1985), intra-oceanic island arcs (e.g., Nivia, 1996;

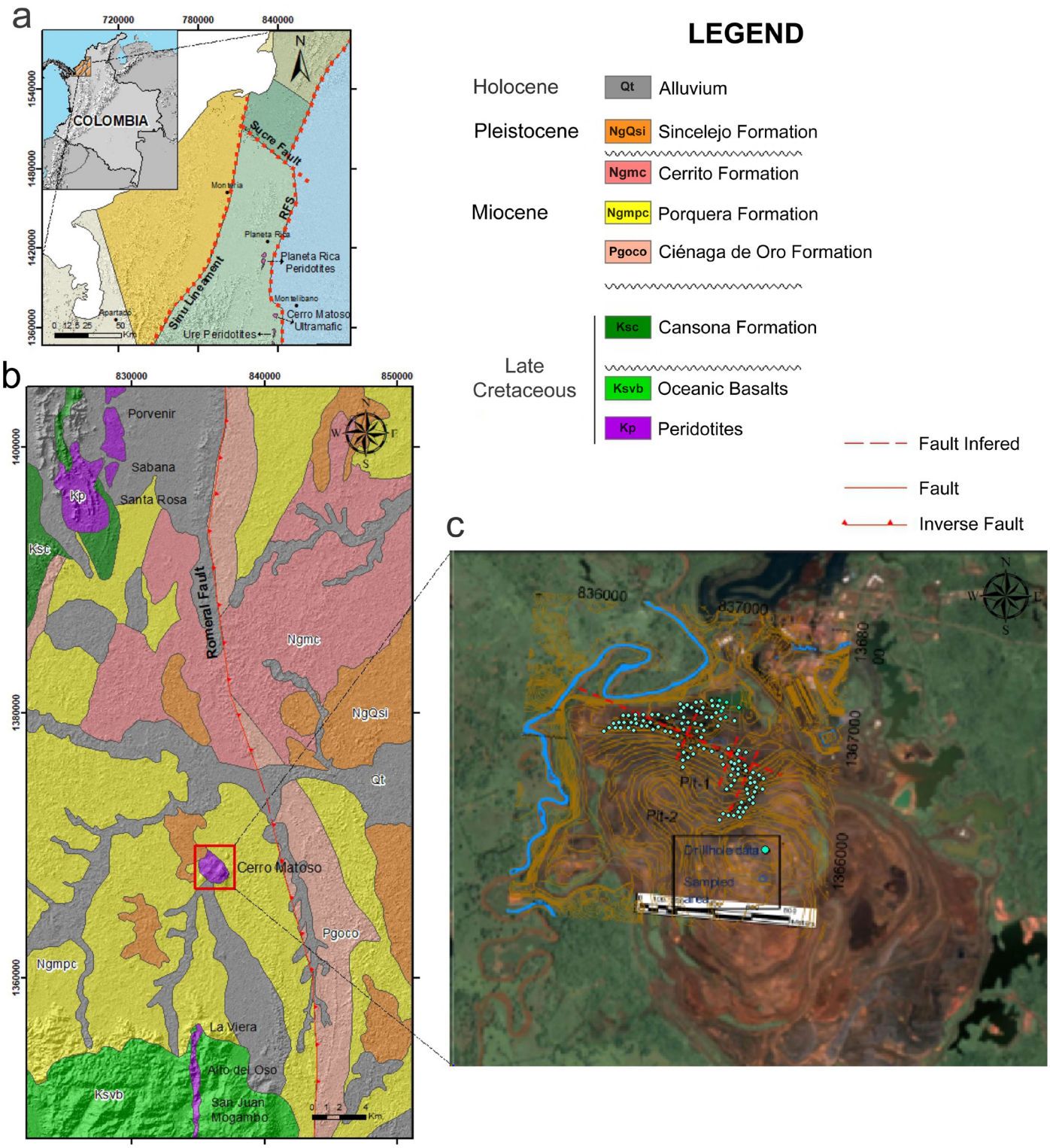

Fig. 2 - a) Regional geology and location of Pit-1 in the Cerro Matoso mine. b) The Late Cretaceous Cerro Matoso peridotites are unconformably covered by upper Oligocene to Pleistocene strata, including the Ciénaga de Oro (Pgoco), Porquera (Ngmpc), Cerrito (Ngmc), and Sincelejo (NgQsi) Formations. Modified from the SGC Geological maps 72 and 82 (Pueblo Nuevo and Montelibano) and from Tobón et al. (2020). c) Cyan dots show the sedimentary distribution of the Black mudstones at Pit-1 with a thickness varying between 10 to 20 m.

Spadea and Espinosa, 1996) and the Caribbean Plateau (e.g., Nivia, 1996; Kerr et al., 1997). Cerro Matoso was assigned as part of the Cauca Ophiolitic Complex, tectonically emplaced west of the Romeral Fault System during the Early Cenozoic Pre-Andean orogeny (Mejia and Durango, 1981; Gleeson et al., 2004).

The Cerro Matoso peridotite hillsides are unconformably covered by strata of Early and Middle Miocene age, which include a transgressive succession composed of fluvial and shoreface sandstones of the Ciénaga de Oro Formation, followed by the marine shales of the Porquera Formation.

The oceanic crust segments accreted to the western edge of the South American Plate are part of what Nivia (1997) called the Western Cretaceous Oceanic Lithospheric Province (PLOCO, Provincia Litosférica Oceánica Cretácica Occidental). Mejía and Durango (1981) assigned the Cerro Matoso ultramafic rocks to Early Cretaceous whereas, according to Dueñas and Duque (1981), the Planeta Rica Peridotites, located 30 km north were accreted during the Late Cretaceous. Most likely, the emplacement of Cerro Matoso and Planeta Rica peridotites took place during the pre-Andean orogeny (Middle Eocene) and from that moment, the laterization process began (Dueñas and Duque, 1981; López-Rendón, 1986; Hoyos and Velázquez, 1996).

The Planeta Rica Peridotites that developed an incipient laterite profile, are associated with cherts of Campanian age (Dueñas and Duque, 1981) which provide a better base for dating than the Cerro Matoso peridotites, which lack datable fossil material. It cannot be excluded that both were accreted during the late Maastrichtian and Early Cenozoic. The Planeta Rica Peridotites are also covered unconformably by the Ciénaga de Oro and Porquera Formations (Fig. 2b).

CERRO MATOSO GEOLOGY AND MINERALOGY

López-Rendón (1986) characterized the Cerro Matoso peridotites as harzburgites with dunite dikes accompanied by uneconomic chromite lenses, whereas Gleeson et al. (2004) assess: "*The protolith is dominated by forsteritic olivine, diopside, enstatite, chromite, and iron oxides and can be classified as predominantly lherzolitic in composition but with pods of dunite and harzburgite*". According to Lewis et al. (2006) these peridotites are comparable to the Mediterranean-type ophiolites described by Dilek (2003).

According to López-Rendón (1986) the lateritic profile at Cerro Matoso consists of 5 main units from base to top: unaltered peridotites, saprolitized rocks, saprolites, limonites, and iron hat or ¨duricrust¨. These main units comprise several rock types and mineral zones, which can be distinguished depending on their physical appearance, chemical, and mineralogical composition. Gleeson et al. (2004) studied two typical alteration profiles at Cerro Matoso, one developed on Pit-1 toward the N sector of the mine and the other one on Pit-2 toward the S sector. In both sectors, they identified pimelite and sepiolite as the major nickel-bearing silicate phases, followed by smectites (saponite) and chlorites (nimite) (Fig. 2c). The lateritic profile at Pit-1 that reach 8-9 wt% Ni grade is composed, from base to top of peridotites, saprolitized peridotites, green saprolites (high and low Mg), brown saprolites, laterites, and duricrust. In the S sector, the Pit-2 peridotites developed a thinner lateritic profile, similar to that of other lateritic bodies in the Caribbean, with an altered profile formed of peridotites, saprolitized peridotites, high and low-magnesium green saprolites, brown saprolites, and high and low iron laterites, without ferricrete or duricrust cover and with a lower Ni enrichment grade (< 4 wt%). Seven horizons have been described in the laterite profile of Cerro Matoso at the Pit-1 (Gleeson et al., 2004; Tobón et al., 2020), nevertheless, the horizons at the top: ¨*black saprolite*¨, ¨*red laterite*, and ¨*canga mona*¨ were redefined as deep marine sediments by Castrillón, (2019).

ANALYTICAL METHODS

A representative set of 22 samples was collected at the 49 Bench level of Pit-1 where the marine sediments are exposed on top of the peridotites. The black mudstones can occur as two varieties (A: CM19 and B: CM26 samples) (Table 1, Fig. 3a-c and f). These sediments overlie listvenites, which also present two varieties (Fig. 3d and e). The listvenites cap green saprolites (Fig. 3g and h). Downwards, the laterite profile consists of altered peridotites (Fig. 3i), peridotites with magnesite veins (Fig. 2j) and fresh peridotites (Fig. 3k-l). Subsamples for analyses were extracted from the internal regions of the original rock sample to avoid contamination (Nan et al., 2021). All subsamples were cleaned and subdivided into polished, resin-free rock chips and freshly broken fragments. Petrographic study was carried out using binocular and petrographic microscope Carl ZEISS Primo Star HD / Full Köhler cam, 100x, from the Instituto de Geología of the Universidad Nacional Autónoma de México (UNAM). XRD analyses were performed in Ciudad de México. For the whole-rock mineralogical analysis, samples were grounded with an agate pestle and mortar to < 75 μm and mounted in aluminum holders for X-ray powder diffraction analysis. Measurements were made using an EMPYREAN diffractometer at Instituto de Geología, Universidad Nacional Autónoma de México. The UNAM equipment operated with an accelerating voltage of 45kV and a filament current of 40mA, using CoKα radiation (cobalt tube), without monochromator and iron filter in the optical incident part of the equipment; the detector used was of solid-state (PIXCel 3D). The preparations in the UNAM labs were measured over a 2θ angle range of 5-80° (air-dried) and 5-40° (glycolate and heated) in steps of 0.003- and 40-seconds integration time. Peak positions were standardized against quartz 100 peaks of relative intensity taken at 4.26 Å. Databases used for identification were ICCD (Inorganic Crystal Structure database) and ICDD (International Center for Diffraction Data).

Table 1 - Summary of samples collected in Cerro Matoso, Bench 49 Pit-1.

Rock name	CM sample id	Total
Orange Iron laminated claystone	46	1
Red claystone	13	1
Black mudstone	19, 20, 26	3
Intraclast	1, 2, 5, 9, 35	2
Listvenites	3, 4, 6, 7, 18, 27	6
Green Saprolite	12, 34	2
Saprolitized Peridotite	15, 17, 28, 30	4
Peridotite	16, 29	2
Serpentinized Peridotite	14	1

Fig. 3 - Hand samples collected from the Cerro Matoso deposit at Pit-1. a,b) Black mudstone facies II. C,f) Black mudstone facies II. D) Listvenite variety B, characterized by a purple color. e) Listvenite variety, characterized by brecciated texture with high silica/siderite vein content. g) Low-Mg green saprolite. h) High-Mg green saprolite. i) Saprolitized peridotite. j) Magnesite and silica veins in peridotite. k) Fresh peridotite. l) Serpentinized peridotite.

Profiles and phase identification and Rietveld Refinement were made with a PDF-2 database using Highscore v.4.5 Software. A Hitachi-TM-1000 wd/ed scanning electron microscope, in combination with a JXA-8900R microanalyzer, both from the UNAM Instituto de Geofísica Ambiental, allowed us to obtain back-scattered electron (BSE) images and qualitative chemical analyses by energy dispersive X-ray spectrometry (EDS) in samples of black mudstone I facies (Sample_CM26) and black mudstone II facies (Sample_CM19). The analytical condition included acquisition time of 29 s, processing time of 4 min, and voltage of 15 kV. Standards used for calibration of the equipment comprised pure metals and synthetic and natural minerals (carbonates and sulfates) from the set of standard SPI # 02753-AB serial No. 02-148. To confirm REE results from EDS data, bulk-rock analyses of element concentrations of subsamples CM19 and CM26 were carried out by a combination of ICP-MS instrumental analysis (i.e., package Code UT-5) at the commercial laboratory ACTLABS. Standards measurement conditions and detection limits are described in the 4Litho report (https://actlabs.com/geochemistry/exploration-geochemistry/multi-method-analysis). The Rock-Eval-6/TOC pyrolysis analysis, and maturity test, were performed in ANTEK laboratories, which provided a source rock analysis (SRA)_Leco TOC for samples CM19 and CM26. For this analysis, 100 mg of sample were heated to 300°C to release volatile hydrocarbons (S1). Later, the pyrolysis sample was

run at a rate of 25°C per minute until reaching 600°C, to release pyrolytic hydrocarbons (S2). The released CO_2 was trapped inside a thermal conductivity detector to obtain the amount of total organic carbon (TOC) produced thermally (S3).

RESULTS

Field observations

An irregular and pseudostratified characteristic package of approximately 40 m in thickness is overlying the peridotites and listvenites at Cerro Matoso Pit-1. This unit of prevalently blackish colour is characterized by brittle, granular appearance, mud-sandy texture, fossil contents, a huge intraclast content and by the occurrence of goethite, and magnetite. The intraclasts are of different sizes (i.e., fragments of peridotite and claystone with a range size from granules to pebbles) including some boulders of serpentinite and claystone rock fragments (Fig. 4a, 4d and e). The full packages change upwards along with transitional contacts and can be divided into several facies from the base to the top: black mudstone (BM) facies, with two varieties (BM I and BM II facies), red claystone facies (RC), and orange iron laminated claystone facies (oil-C) (Fig 4B). Usually, the black mudstone is overlying listvenites, i.e., metasomatized peridotites (Fig. 4c).

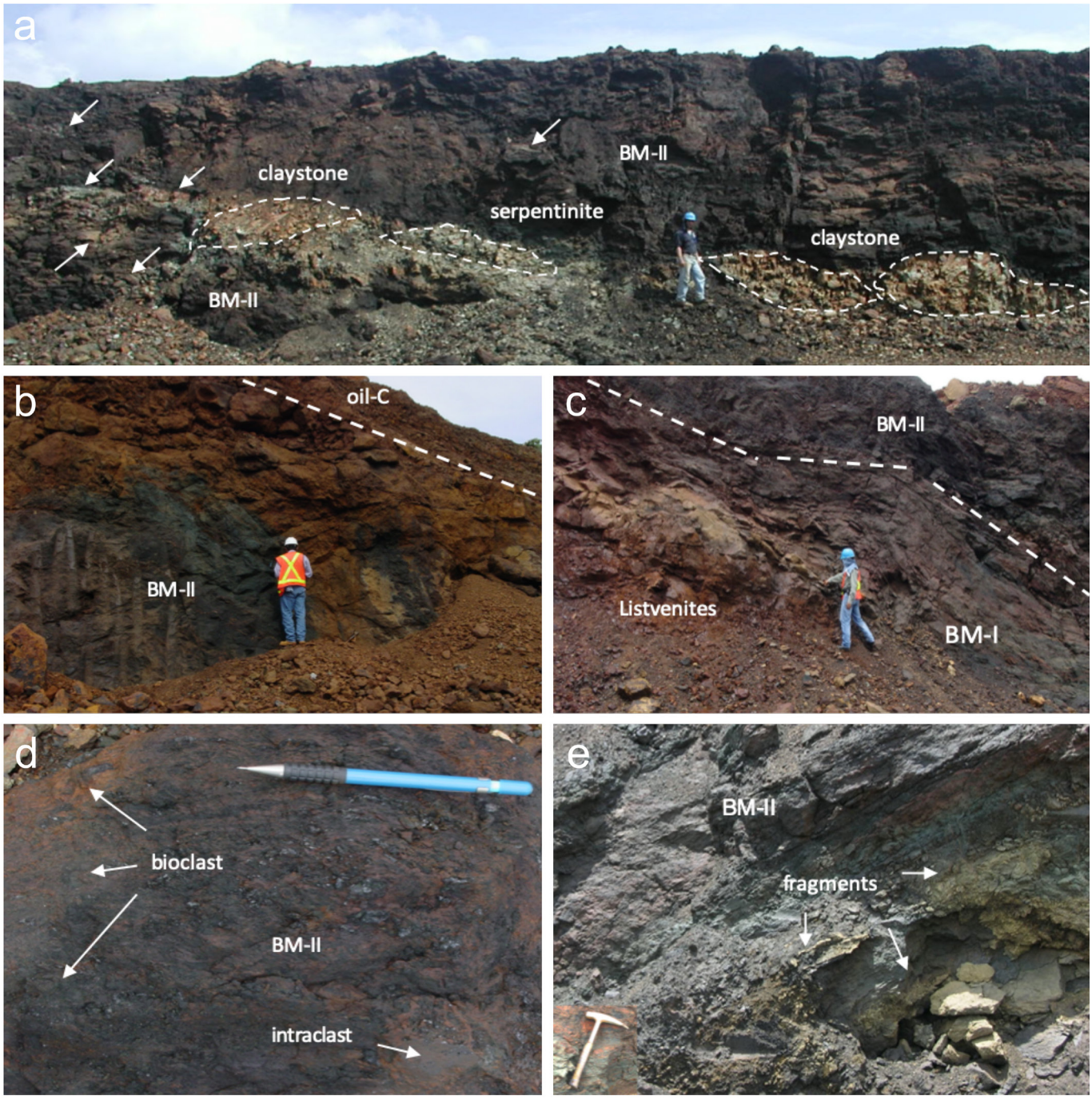

Fig. 4 - a) Serpentinite and claystone boulders into black fine laminated mudstone II facies (BM-II). b) orange iron laminated claystone (oil-C) overlying black mudstone facies. c) Black mudstone facies varieties (BM I and BM II) overlying listvenites. d) intraclast and bioclast forming black mudstone II facies. e) Fragments of peridotites and claystone with a range size from granules to pebbles into the BM II unit.

The black mudstones are fossiliferous, friable, granular in appearance, and with a muddy-sandy texture; the two facies differ principally in the bluish-green to very pale green color of BM I facies (Fig. 5b-c) vs the dominant black colour and magnetite content of the BM II facies (Fig. 5a-c). Both facies also are characterized by a framework composed of bioclasts and intraclasts. In general, all rocks are enriched in oxides (e.g., chromite, goethite) and oxides-hydroxides with different amounts of Mn (e.g., manganite, pyrolusite).

Petrography

In thin section, the framework of the BM facies II is formed by fine sand size to coarse silt size particles and fragments of organic structures exhibiting irregular shapes that were replaced by Fe-oxides and siderite (Fig. 6a). The percentage of bioclast (i.e., gastropod shells) reaches 40 vol% and their state of conservation is poor. According to XRD analysis (Table 2), the clayish matrix is composed of the assemblage greenalite-nimite. Goethite-magnetite were also detected by XRD (Fig. 6b). Two types of intraclasts were distinguished: reddish-couloured intraclasts composed of phyllosilicates (greenalite + berthierine) + siderite replacing organic fragments and infilling pores spaces + minor hematite and oxides with fluid textures (Fig. 6c), and greenish-coloured intraclasts composed of ultramafic fragment of serpentine, clinopyroxenes relics, siderite and oxide, these latter as cracks filling (Fig. 6d).

SEM analyses

Backscattered electron images of black mudstone I facies (Sample CM26) show the clayish fraction (< 2mm) containing disseminated white and black particles detected under a 200 mm scale (Fig. 7a and 8a). The white color fine silt size particles (< 20 mm) are angular crystals which, according to the chemical composition and habit, correspond to nimite with a nickel content of 9.6 wt% (Fig. 7b). The fine to very fine silt size opaque black particles (< 10 mm in diameter approx.) are circular to ovoid, surrounded in edges with irregular shapes and shells appearance (Fig. 7c-e). In Fig. 8a the black particles within the clays can be observed surrounding a shell print. Detailed characteristic of ovoid and circular fine silt size particles is shown in Fig. 8b and c, while particles of irregular forms are in Fig. 8d and e. Clay size particles covering the organics correspond to halite (Fig. 7d,e and 8c).

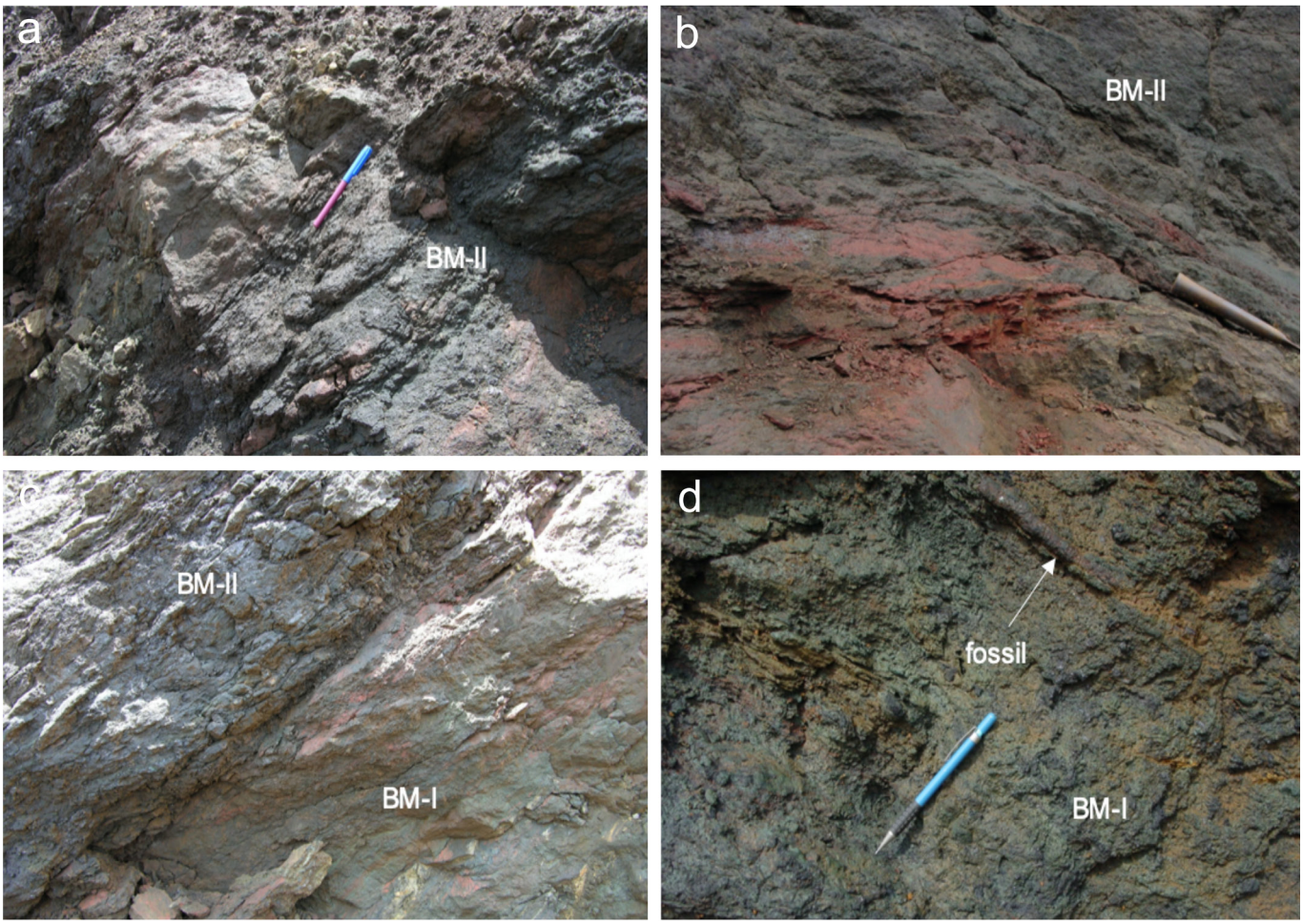

Fig. 5 - A-B) Detail of the black and red colours of BM II facies, which also show the fine to coarse usual lamination and fine and discontinuous beds. C) Field relations among BM I mudstone facies usually underlying the BM II facies. D) fossil of tube structure in the BM I facies with characteristic blue-greenish colors.

Table 2 - XRD mineralogy of Black mudstone I and II facies (samples CM26 and CM19).

Facies Name	Hand Sample Description	Principal minerals XRD (Castrillón. 2019)	Sample Id	Dust Fraction		Clay Fraction	
				Pos 2The	FWHM	Pos 2The	FWHM
Black mudstone II	Fine sand to coarse silt size and friable rock with muddy texture. Dark bluish green (5BG 3/2) and very pale green (10G 8/2) colored. Clayish matrix. Magnetic.	greenalite. nimite. siderite. goethite. magnetite. chromite. Fe_oxide. tosudite	CM-19	14.43	0.17	14.44	0.23
			54	14.43	0.17		
			19	14.48	0.16		
Black mudstone I	Clayish rock mottled in appearance. Green (10G 8/2) to pale green (5G 7/2) colored. alternating with non-continuous orange. red. and black laminations associated to Fe oxides and manganese.	greenalite. berthierine. siderite. goethite. manganese oxide. nimite.	CM-25	14.21	0.19	14.24	0.13
			26	14.28	0.29		
Serpentine intraclast	Weakly foliated massive hard rock of pale yellowish green in color (10GY 7/2) with phaneritic texture and weakly oriented mafic of very coarse sand size.	siderite. antigorite. olivine. talc. serpentine. spinel.	9				
Claystone intraclast	Claystone well cemented. Moderate reddish brown (10R 4/6) and mottled in color.	greenalite. berthierine. siderite. goethite. nimite. chromite	CM-27	14.18	0.23	14.26	0.17
			35	14.18	0.4		

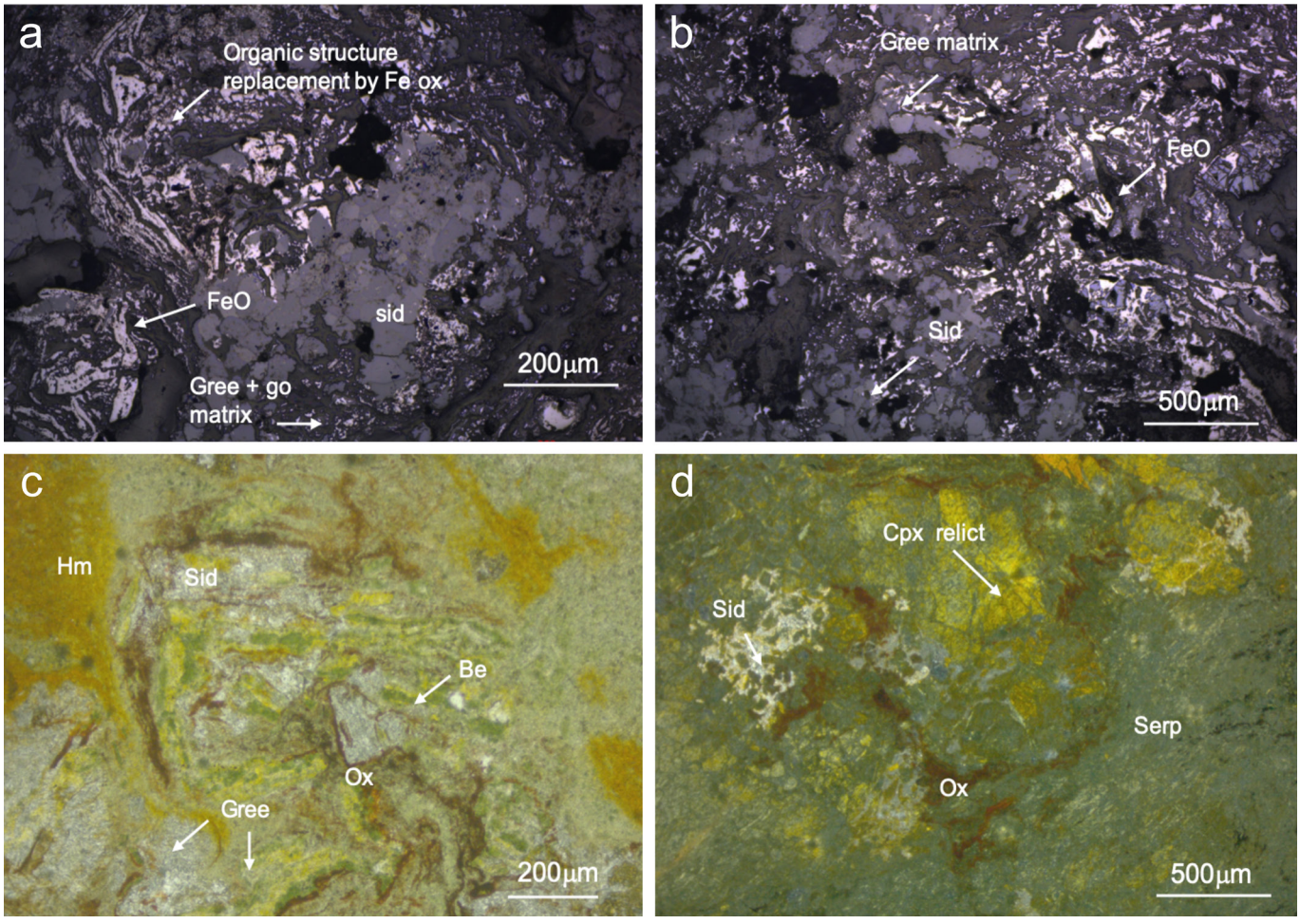

Fig. 6 - Thin sections: a,b) Fe-rich oxides (ox) forming black mudstone II facies; organic structures are replaced by hematite (white) and siderite in a matrix formed by greenalite (Gree) + goethite (go). Sample CM19_10_10x_lt. c) claystone fragment formed by a matrix of greenalite, berthierine (Be), siderite (sid), hematite, and hematite. Sample CM01_13_10x_nc. d) Serpentine fragment (serp) composed of clinopyroxene relict, siderite filling cracks and oxides. Sample CM05_2_5x_nc.

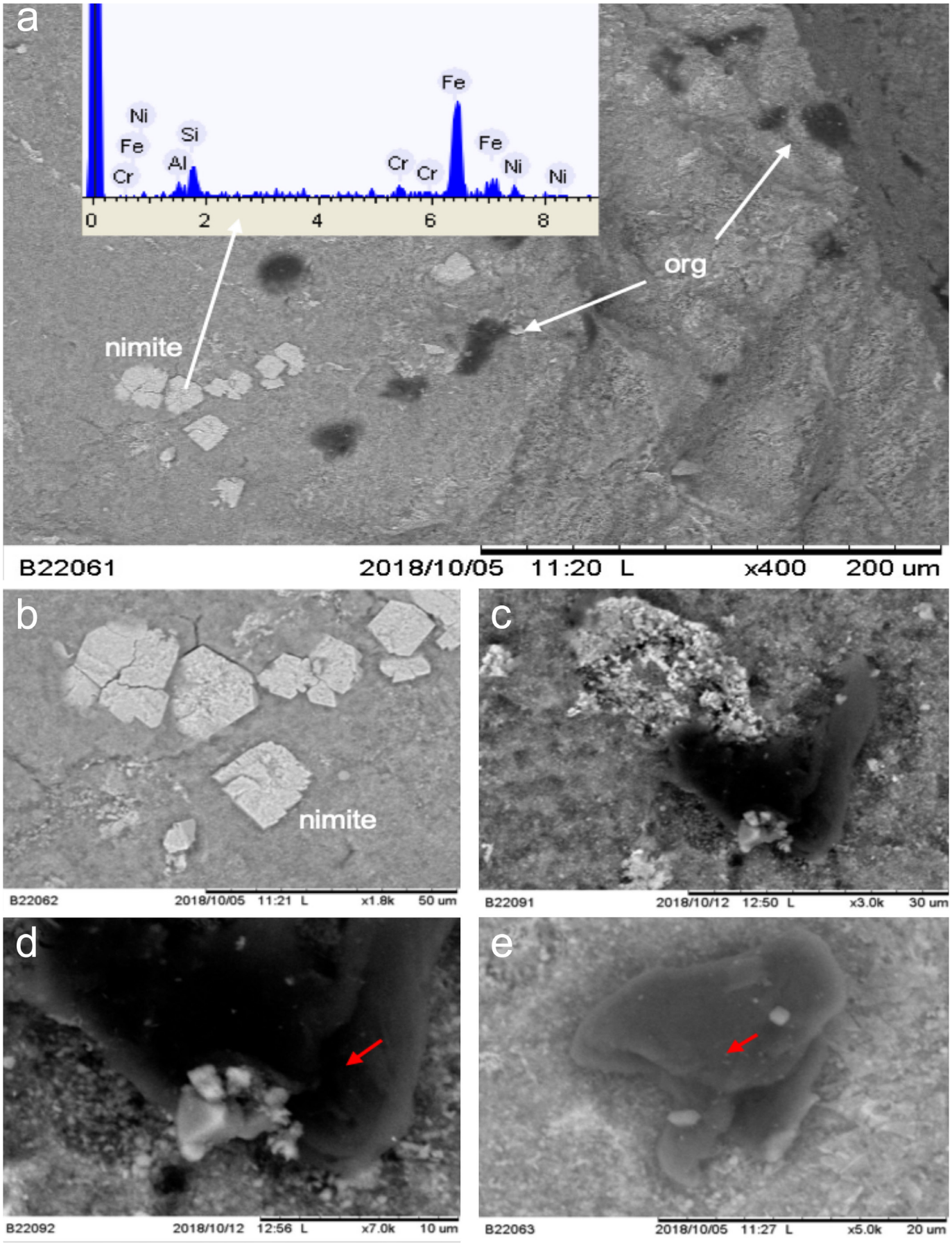

Fig. 7 - Backscattered electron image of black mudstone I facies, sample CM26_2A. a) Whole image of 0.4 mm length with clays, pseudo-hexagonal crystals of nimite (white) and organic aggregates (black) within the clays. b) Detail of fine silt size crystals of nimite, registering a nickel content of 9.6% (see sample CM26A-Table 1). c) Detail of fine silt size organic particle with rounded edges. Nickel content in aggregates reach 4.2 wt%. Sample CM26_3. d) Detail of the organic aggregates fine silt particle with halite crystals inside. e) Detail of fine silt size organic particle with rounded edges and biogenic appearance.

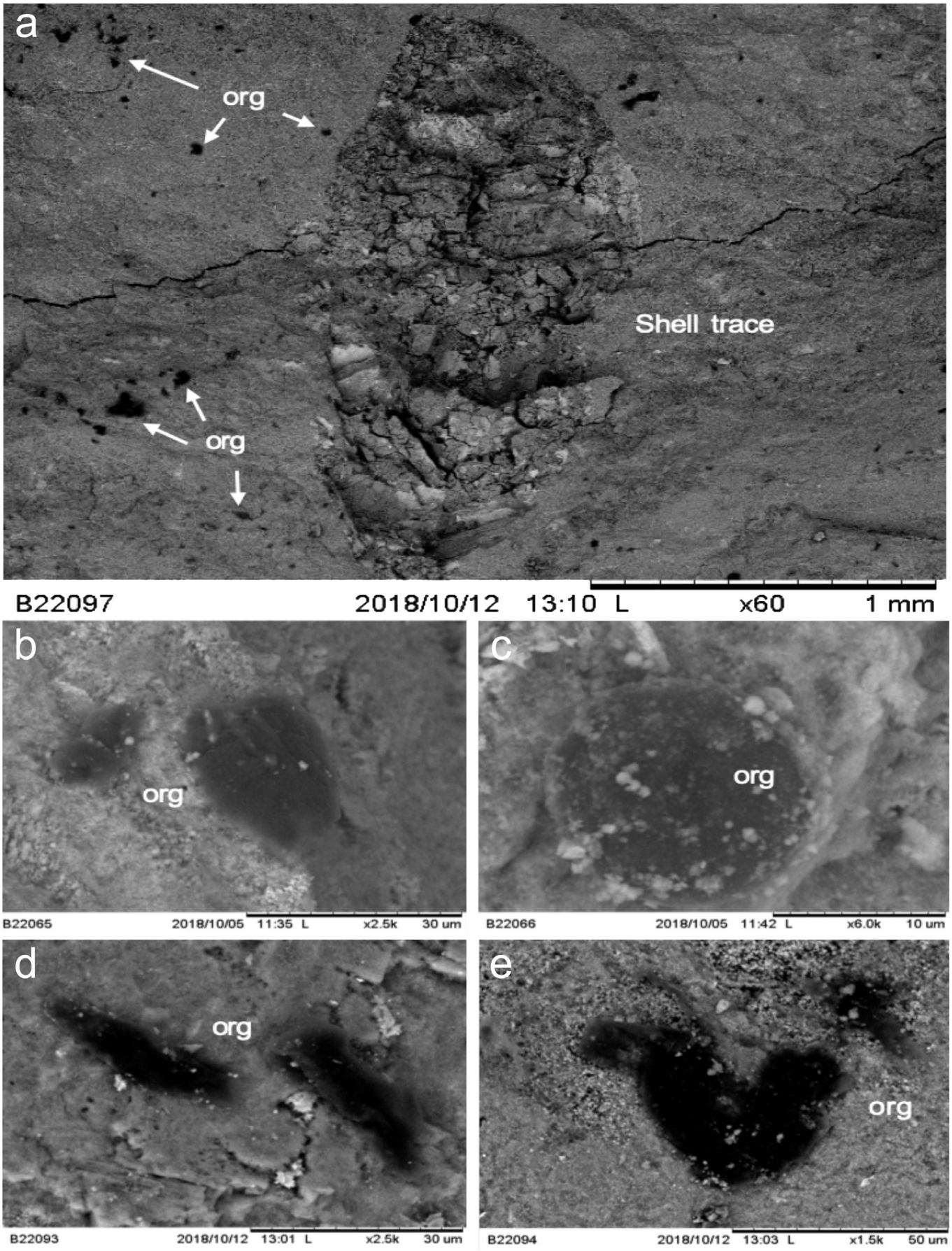

Fig. 8 - Backscattered electron image of black mudstone I facies, sample CM26_2A. a) Whole image of shell trace (very coarse sand size) with fine to very fine size particles of organic aggregates within the clayish matrix; the Ni in the clayish matrix reaches 2.4 wt%. b) Fine and very fine silt size particles of organic aggregates with 9.1 wt % of Ni; sample_CM26-6. 8c and 8d) Very fine silt size particle of rounded organic with biogenic appearance with 7.1 wt% of Ni; sample_CM26-4. E) Medium silt size particle of organic with irregular forms.

EDX analyses obtained above the surface of organic particles for sample CM26 reveal the presence of nickel (4.2-9.1 wt%), iron (58.6-87.5 wt%), chromium (2.1-4.6 wt %), silicon (5.4-10.4 wt %), aluminum (1.7-2.5 wt%), plus Cl (7.2 wt%), Na (4.1 wt%) and K (2.4 wt%) as part of the organic envelopes (Fig. 9a) and of the matrix (Fig. 9b). EDX analyses on particles forming the sample CM19 indicate a matrix composed of Al, Fe, Cr, Si, and Ni that are contained in phyllosilicates (i.e., greenalite + nimite). These clayish particles contain iron (81.6-84.8 wt%), nickel (2.6-4.2 wt%), chromium (1.1-2.6 wt%), silicon (3.0-4.1 wt%) and aluminum (4.3-9.7 wt%) (Table 3). Ni in the clayish matrix vary in the range 4.2-5.4%. In addition, coarse silt size particles correspond to idiomorph Fe-Mn berthierine with 2.6% of Ni (Fig. 10b-c), and other coarse silt size particles correspond to magnetite fragments (Fig. 10c). Fine silt size particles of black opaque circular to ovoid organics are also detected in the BM II facies (Fig. 10b). Tosudite identified with XRD crystallized as films with Ni content of 1.5% covering greenalite aluminosilicate fine silt size grain (Fig. 11). Also, coarse silt size shell particles are recognized.

ICP-MS

Bulk sediment chemical TD-ICP- MS analyses of samples CM26 and CM19 (Table 4) confirms high values for typically "ultramafic elements" apart from Fe and Mg: Ni 12500-14400 ppm, Mn > 10000 ppm, Co 2600-3040 ppm, Cr 9670-17500 ppm, V 89-716 ppm, Zn 353-407 ppm and Cu 129- 246 ppm. The REE contents are close to the "average shale" (Piper, 1974) with exception of La, Ce, Pr. Th, K, and Ag are under the detection limit. Cu, Zn, Co, Cr, and V are highest in the basal unit or BM I facies (sample CM26) than in the BM II facies (sample CM19). Normalized to Post-Archean Australian Shales (PAAS) both samples display a relative Eu enrichment ([Eu/ Eu*]SN of 1.37 and 1.45 for samples CM19 and CM26, respectively (Fig. 12a).

TOC

Total organic carbon contents in the black mudstone facies BM-I and BM-II facies (Table 5) are 0.05 and 0.03 wt% for samples CM26, CM19 respectively. The carbonate content for each sample is 57.3, and 84.7 vol% respectively. The rock-Eval results show 7.5 and 3.9 mg CO_2/g in each sample.

DISCUSSION

Hydrothermal imprint characteristics

The organic aggregates chemical composition obtained in EDX indicates an envelope composed of phyllosilicates (i.e., with Al, Fe, Si) with Ni and Cr in their structure. Elements such Th, Pd, Ag, As and Sb detected in some organics with EDX were not confirmed by TD-ICP-MS analyses. This indicates that organic particles do not belong properly to serpentinites, which are characterized by high concentrations of As and Sb, when they host black smoker vent fields (Marques et al., 2006; Andreani, et al., 2014). In contrast, REE elements detected in ICP-MS analyses point out that samples and therefore the inner organic particles are associated with marine sediments affected by hydrothermal influence.

REE displays a positive Eu anomaly [Eu/ Eu*]SN ratio of 1.37 and 1.45 (normalized to Post-Archean Australian Shales-PAAS) that indicate a removal activity of ocean water particles and a dilution of a hydrothermal fluid signature. These results coincide with those collected in the hydrothermal fluids of Yonaguni Knoll IV with a typical enrichment of Eu and a systematic heavy REE increase reported for mid-ocean ridges (Hongo et al., 2007). Additionally, REE/Fe ratios of BM I ($3.3 \cdot 10^{-4}$) and BM II ($1.7 \cdot 10^{-4}$) facies are quite similar to REE/Fe ratios of the Rainbow hydrothermal field particles (REE / Fe - $1.6 \cdot 10^{-4}$) (Chavagnac et al., 2005) which is a deep-sea ultramafic body that could be compared with the Cerro Matos peridotites (Fig. 12b). The REE patterns could be also compared with those of iron formations or BIFs (Paleo- and Neoproterozoic), which present a mineralogic association (i.e., greenalite + siderite) similar to BM I facies, but characterized by high LREE/HREE ratios and positive Eu anomalies, that have been interpreted as originated from hydrothermal sources in a mid-oceanic ridge setting (Beukes and Klein 1990, Bau and Dulski, 1999; Johnson et al., 2003).

Similar REE patterns with positive Eu anomaly are reported from hydrothermal plume-derived iron oxide sediments in the TAG hydrothermal field, Mid-Atlantic Ridge- MAR; in the Rainbow vent field of the MAR; in the Ordovician jasper from the Løkke district, Norway; and in the Jurassic jasper from ODP Site 801C in the western Pacific Ocean (Slack et al., 2007). Paulick et al. (2006) and Andreani et al. (2014) report similar REE patterns only for serpentinites originated from such abyssal hydrothermal vent fields. LREE enrichments and Eu anomalies are associated to high sulfide abundance.

Table 3 - EDX chemical composition of the Ni-ore in the black mudstone I and II facies in Cerro Matoso.

Sample	CM26A	CM26 3	CM26 4	CM26 6	CM26 8	CM26 10	CM19-1	CM19-9	CM19-10	CM19-7A	CM19-7B
Phase	Nimite Fig. 7b	Org Fig. 7c-d	Org Fig. 8d	Org Fig.8b	Org Fig. 9a	Clay Fig. 9b	Clay Fig. 10a	Berthierine Fig. 10b	Berthierine Fig. 10c	Grain Fig. 11	Film Fig. 12
(element, wt%)											
Al	1.7		1.3	1.3	2.5	2.8	4.3	6.1	9.7	3.0	2.4
Si	5.6	6.1	5.6	5.4	10.4	8.0	4.1	3.6	3.0	3.1	2.8
Cr	3.6	2.2	3.7	4.6	3.1	4.1	2.6	1.5	1.1	23.3	2.1
Fe	79.5	87.5	82.3	79.7	58.9	77.5	84.8	81.6	82.3	70.7	90.5
Ni	9.6	4.2	7.1	9.1	4.5	5.4	4.2	2.6	2.6		1.5
Na					4.1						
Cl					7.2						
K					2.4						
Ca					1.1						
Mn								4.7	1.3		0.7

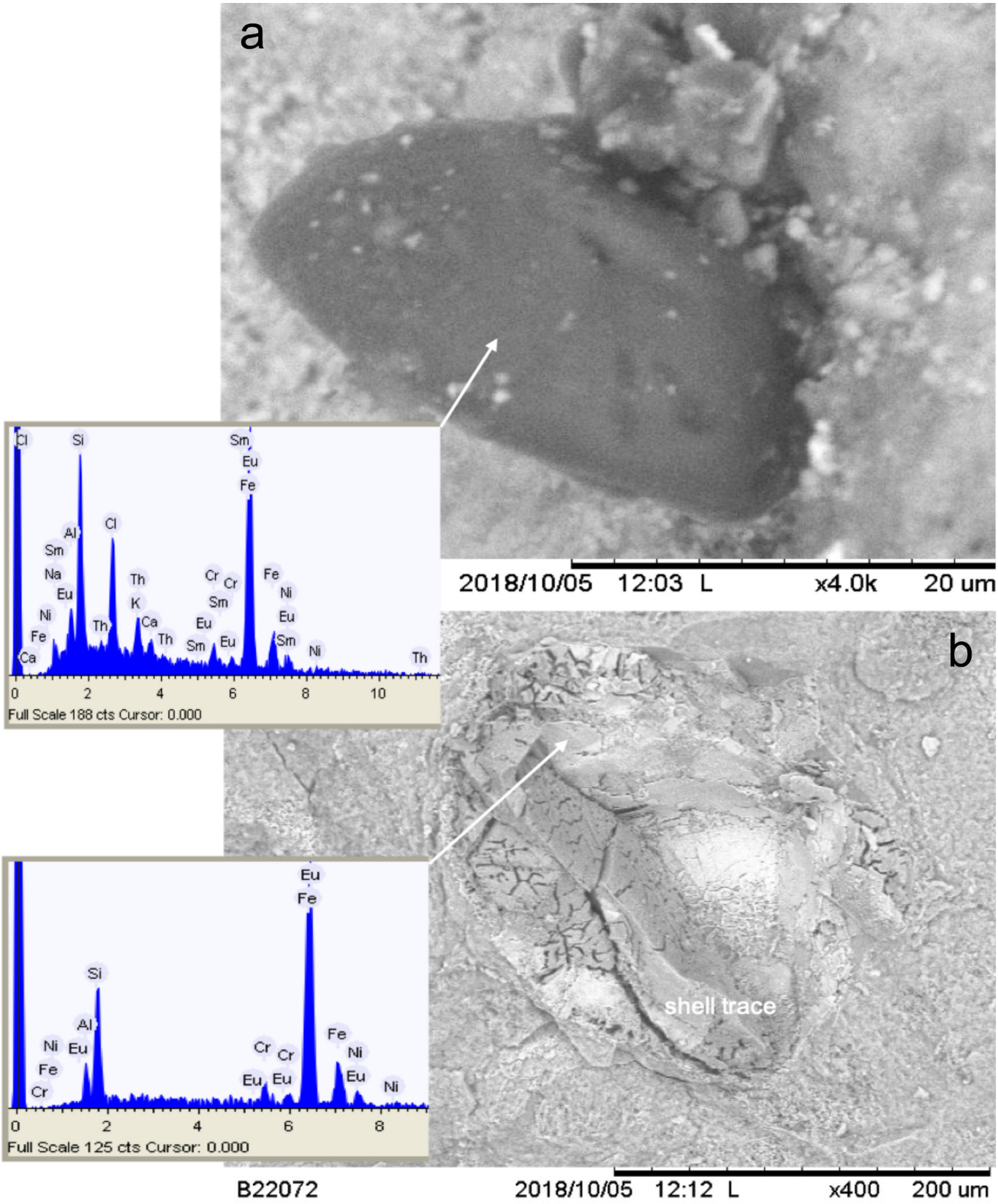

Fig. 9 - Backscattered electron and EDX images of black mudstone I facies. a) Medium silt size particle of organic structure, with rounded shape and shell appearance composed of Al, Fe, Cr, Ni, Na and K, and possible REE elements. Sample CM26-8. b) Fine sand size shell print in the clayish matrix indicating an Eu content, the clayish matrix has a Ni content of 5.4 wt%, sample CM26-10.

Table 4 - Chemical composition of bulk samples from black mudstone II and I facies.

Analysis Method	Detection Limit	Analyte Symbol	Unit Symbol	CM19 BM II	CM26 BM I
TD-MS	0.01	Ca	in %	0.03	0.06
INAA	0.01	Fe		46.1	38.4
TD-MS	0.01	Mg		0.66	0.72
INAA	0.01	Na		< 0.01	0.01
TD-MS	0.01	K		< 0.01	< 0.01
INAA	2	Au	in ppb	< 2	< 2
TD-MS	10	Hg		< 10	130
MULT INAA/TD-ICP-MS	0.05	Ag	in ppm	< 0.05	< 0.05
TD-MS	0.2	Cu		129	246
TD-MS	0.1	Cd		1	1.3
TD-MS	1	Mn		> 10000	> 10000
TD-MS	0.5	Pb		< 0.5	0.5
MULT INAA/TD-ICP-MS	0.5	Ni		12500	14400
MULT INAA/TD-ICP-MS	0.5	Zn		353	407
MULT INAA/TD-ICP-MS	1	Ba		7	12
TD-MS	0.1	Be		0.8	2.3
TD-MS	0.02	Bi		< 0.02	0.03
MULT INAA/TD-ICP-MS	0.1	Co		2600	3040
INAA	2	Cr		9670	17500
TD-MS	0.1	Ga		4.2	4.8
TD-MS	0.1	Ge		1	0.6
TD-MS	0.5	Li		0.9	1
TD-MS	0.05	Mo		1.13	1.44
INAA	0.1	Sc		39.3	55.7
MULT INAA/TD-ICP-MS	0.1	Se		0.2	0.6
TD-MS	0.2	Sr		1	2.4
TD-MS	0.1	Te		0.2	0.3
TD-MS	0.05	Tl		0.05	< 0.05
TD-MS	1	V		89	716
TD-MS	1	Zr		2	3
TD-MS	0.1	Y		10.7	17.7
TD-MS	0.1	La		11.5	10.3
TD-MS	0.1	Ce		0.1	0.1
TD-MS	0.1	Pr		5.6	8.3
TD-MS	0.1	Nd		24.4	35.5
TD-MS	0.1	Sm		6.3	9.9
TD-MS	0.05	Eu		1.7	3.02
TD-MS	0.1	Gd		4.4	8
TD-MS	0.1	Tb		0.7	1.6
TD-MS	0.1	Dy		4.5	10.7
TD-MS	0.1	Ho		0.8	2
TD-MS	0.1	Er		2.4	6.5
TD-MS	0.1	Tm		0.4	1.1
TD-MS	0.1	Yb		2.7	8.3
TD-MS	0.1	Lu		0.4	1.2

Note: W, U, Th, Ta, Sb, Sn, Re, Rb, Nb, In, Hf, Cs, Br, As are under the detection limit.

They may be analogous to the sulfide-rich serpentinites and stockworks of modern black smoker systems (Marques et al., 2006; Andreani, et al., 2014, Hodel et al., 2018).

Recently, these LREE patterns and Eu anomalies, were explained by the high mobility of such elements in acidic Cl-rich fluids, due to chlorine complexation at low pH (Hodel et al., 2018). Douville et al. (2002) argued that chlorine complexation caused the ability of such acidic Cl-rich fluids to mobilize and transport significant amounts of transition metals, including iron (forming Fe-Cl complexes), within abyssal hydrothermal systems. Marques et al. (2006) suggested that high chlorinity in vents around ultramafic rocks is not straightforward unless mixing with a high salinity brine or direct contribution from a magmatic Cl-rich aqueous fluid is considered. This pattern could explain the Cl content in some EDX patterns. Perner et al. (2009) examined low-temperature hydrothermal fluid samples with respect to their chemical and microbiological characteristics, finding that fluids entraining microorganisms modify the chemical microenvironment within the subsurface biotopes. In addition, in seawater hydrothermal systems chlorite is associated to other alteration phases, such as brucite and serpentine-chlorite; magnesium-hydroxide-sulfate-hydrate may also precipitate directly from the seawater (Hentscher, 2012).

Table 5 - Rock-Eval-6/TOC pyrolysis analysis, and maturity test in bulk samples of black mudstone I and II facies.

Rock	Sample ID		CM 26	CM 19
Median	Depth	(ft)	4	5
Sample	Type		Powder	
Percent	Carbonate	(wt%)	67.3	84.72
Leco	TOC		0.05	0.03
Rock-Eval-6	S1	(mg HC/g)	0.06	0.04
	S2		0.08	0.06
	S3	(mg CO_2/g)	7.58	3.91
	Tmax	(°C)	430	409
Calculated	%Ro	(RE TMAX)	0.58	0.2
Hydrogen	Index	(S2x100/TOC)	159	233
Oxygen		(S3x100/TOC)	15,100	15,214
S2/S3	Conc.	(mg HC/mg CO_2)	0	0
S1/TOC	Norm. Oil	Content	120	156
Production	Index	(S1/(S1+S2)	0.43	0.4

In addition, Cu and Zn concentrations obtained by ICP-MS, are characteristic of serpentinites from black smoker vent fields due to hydrothermal plume fall out concentration and hydrothermal fluid/rock interactions (Charlou et al., 2002). Both Cu and Zn values, reported by Gleeson et al. (2004) at Cerro Matoso Pit-1, are better explained by hydrothermal veins intruding the mafic/ultramafic rocks. These results support a hydrothermal marine environment as the source for black mudstones at Cerro Matoso instead of the previous interpretation as a part of a supergene laterite profile (e.g., López-Rendón, 1986; Gleeson et al., 2004; Tobón et al., 2020).

In sum, the petrographically and geochemical features of the black mudstones suggest that these sediments were formed at the ocean floor by combined biological and chemical processes enhanced by the interaction of hydrothermal fluids, variable pH conditions, and metal alloys. A deep-sea vent system and reducing conditions related to serpentinization processes of peridotites favour fluid circulation of low to moderate temperatures, alkaline pH (9-11) and production of CH_4 and H_2. In a hydrothermal system Type II of Kelley and Shank (2010), such conditions promote the formation of siderite, Mn-siderite and Fe-phyllosilicates that are components of the Cerro Matoso marine sediments (Castrillón, 2019). According to Laurila et al. (2015), during diagenesis of hydrothermal sediments (e.g., Atlantis II deep ore deposit), within a few meters of burial (corresponding to a few thousand years of deposition), biogenic (Ca)-carbonate is dissolved while manganosiderite is formed, and metals originally in poorly crystalline phases or in pore water are incorporated into diagenetic Fe-oxides, clays, and sulfides.

Microbial activity associated to mantle rocks serpentinization

The extreme environments mentioned above contain a great and unusual microbial activity that permits the ecosystems sustainability (Grossman et al., 2002; Alain et al., 2006; Knittel and Boetius, 2009). Amend et al. (2011) found that in peridotite-hosted hydrothermal systems, compared with their basalt (and felsic rock) counterparts, microbial catabolic strategies and variations in microbial phylotypes may be far more diverse and some biomass synthesis may yield energy rather than imposing a high energetic expense. The consortia formed by these microorganisms have been poorly studied and understood; nevertheless, some studies of the crust in vent settings permitted to recognize consortia as formed by a thick organic matrix (Knittel and Boetius, 2009) with heterogenous shapes and sizes (i.e., 10-20 μm in diameter). They may contain envelopes with thicknesses ranging from 0.5 to 7 mm, permeable, and with limited optical transparent and amorphous minerals on their surfaces (Chen et al., 2014).

The organic compounds can be also synthetized at depth in large exposure of serpentinized rocks without the influence of sediments (e.g., Ménez et al., 2012; Pasini et al., 2013) and get trapped in the serpentinized rocks. An example of abiotic condensed carbonaceous matter CCM within serpentinites is in the Northern Apennine ophiolites outcrops (Emilia-Romagna, Italy): here the carbon abiotic synthesis is formed during serpentinization of diverse mafic and ultramafic mineral precursors and lower temperature ranges (Sforna et al., 2018). Another example of organic matter associated with microbial activity has been referred to a)- disordered carbonaceous matter (DCM) accumulated at the H-Adr interior and filling the grain pits and the microcracks of serpentinized peridotites recovered from the Mid-Atlantic Ridge -MAR, but also to b)- carbon-bearing phase individuated as accumulations wetting the H-Adr grains or specifically interspersed in a complex gel-like mélange of carbon-magnesium-silica filling the H-Adr interior and embedding polyhedral serpentine spherules (Ménez et al., 2012). In both cases, the microscopic organic matter was detected in a completely serpentinized mantle-derived peridotite and is intimately related to secondary mineralization of hydroandraditic garnet (H-Adr) that usually grows over bastite and permit to relate the paragenesis with high pH and Ca^{2+} activity at low O_2 fugacity and temperatures below 200°C (Frost and Beard, 2007, Ménez et al., 2012; Sforna et al., 2018). Similar reduced conditions, high pH, and low-temperature serpentinizing environments, in which the reduction of inorganic carbon to organic compounds is partly driven by the availability of H_2, are suggested for the Cerro Matoso hydrothermal systems. Although some of the aggregate found in the MAR could be similar to the Cerro Matoso, their minerals associations are different from those presented by the organics within black mudstones whose habits correlate better by their shell shapes and mineralogic composition with organics formed by microbial activity into the sediments on top of the peridotites under hydrothermal vent influence. Future investigations will need to determine the functional groups of the organic aggregates of Cerro Matoso.

The particles identified in the black mudstone facies are in forms and morphologies very similar to organic aggregates formed by microscopic consortia. According to the EDX analysis, the aggregates show a high content of Fe, Al, Cr, Ni, Si, and O, indicating phyllosilicates (Fig. 7c) as envelope forming. The EDX Fe-spectra in the aggregates resemble Fe-oxyhydroxides such as ferrihydrite and goethite (Toner et al., 2009) in the same environments. This configuration is similar to Fe-(oxy) hydroxides, and authigenic clays in the Atlantis II Deep of the Red Sea hosted hydrothermal ore deposits (Laurila et al., 2015). According to Chen et al. (2014), the organic clay mineral envelope is a product of bacterially induced mineralization and served as an active interface for the adhesive growth of extra-consortia microorganisms. Clay-encrusted bacteria have been identified in different geochemical

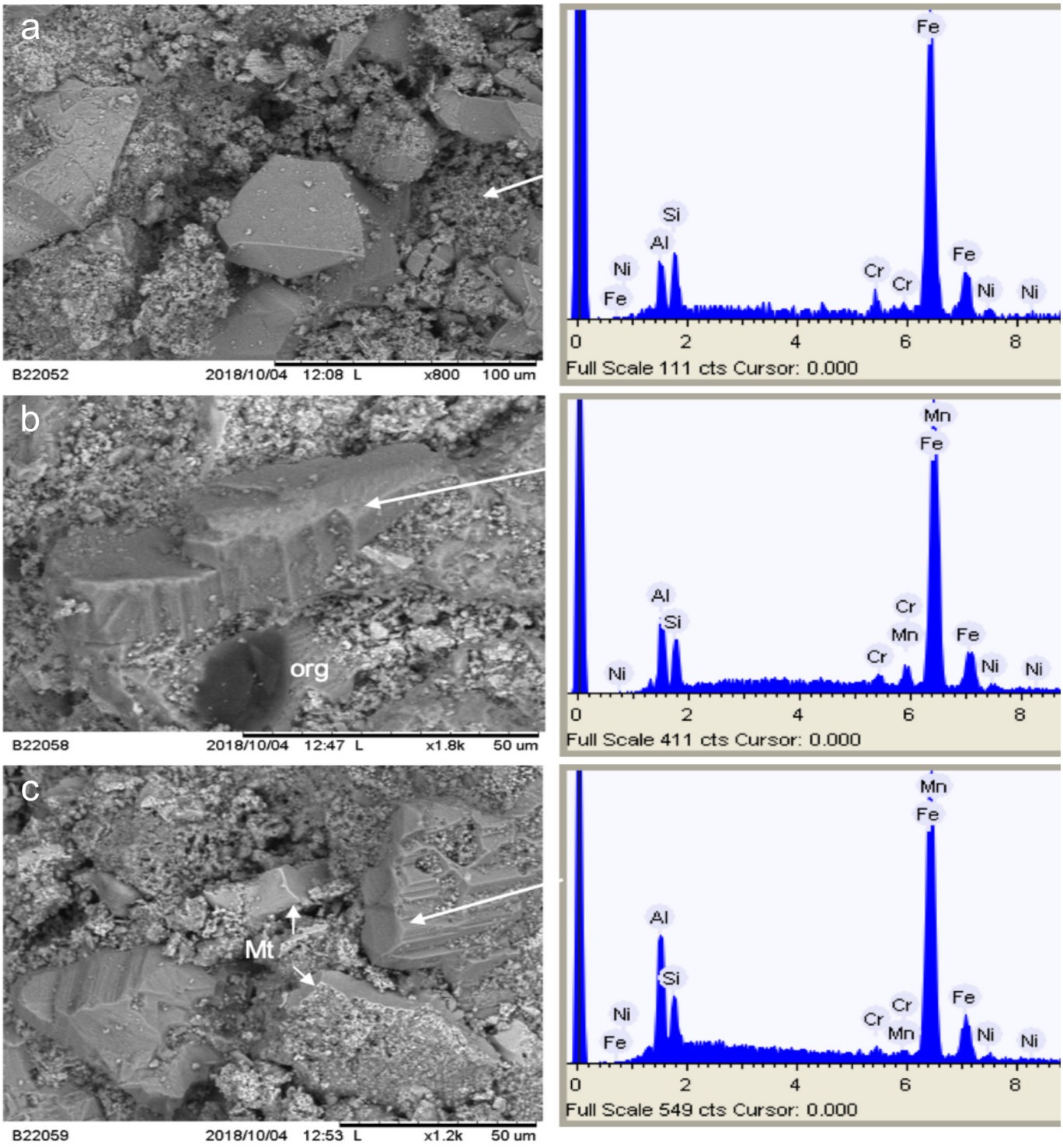

Fig. 10 - Backscattered electron and EDX images of black mudstone II facies. a) The clayish matrix is composed of Al, Si, Fe, Cr and Ni, the latter reaching up to 4.2 wt %. Sample CM19-1. b) Coarse silt size particle of idiomorphic Fe-Mn berthierine with Ni content of 2.6 wt% and fine silt size organic (black) with rounded edges and shell appearance, both forming the mudstone. Sample CM_19-9. c) Coarse silt size particles of idiomorphic Fe-Mn berthierine with Ni of 2.6 wt%, and magnetite. sample CM19-10.

environments, such as the sediments of iron-rich rivers or lakes and in geothermal environments (Ferris et al., 1986; Konhauser and Urrutia, 1999). The described envelope particle composition indicates diagenetic reactions involving fine-grained iron-aluminum silicate minerals, as they are known to play an important role in the solid phase partitioning of metal ions in both marine sedimentary and freshwater systems (Ferris, 2000). Moreover, associated substrate exchange in a hydrothermal environment may occur via the aggregate structure because clay minerals have adsorption and exchange properties with respect to dissolved components (Phoenix and Konhauser, 2008; Ehrlich et al., 2010). The observed disseminated organic aggregates particles can result from an ancient microbial activity supported by the serpentinization of mantle peridotites, and potentially supported by products of serpentinization, as suggested Ménez et al. (2012).

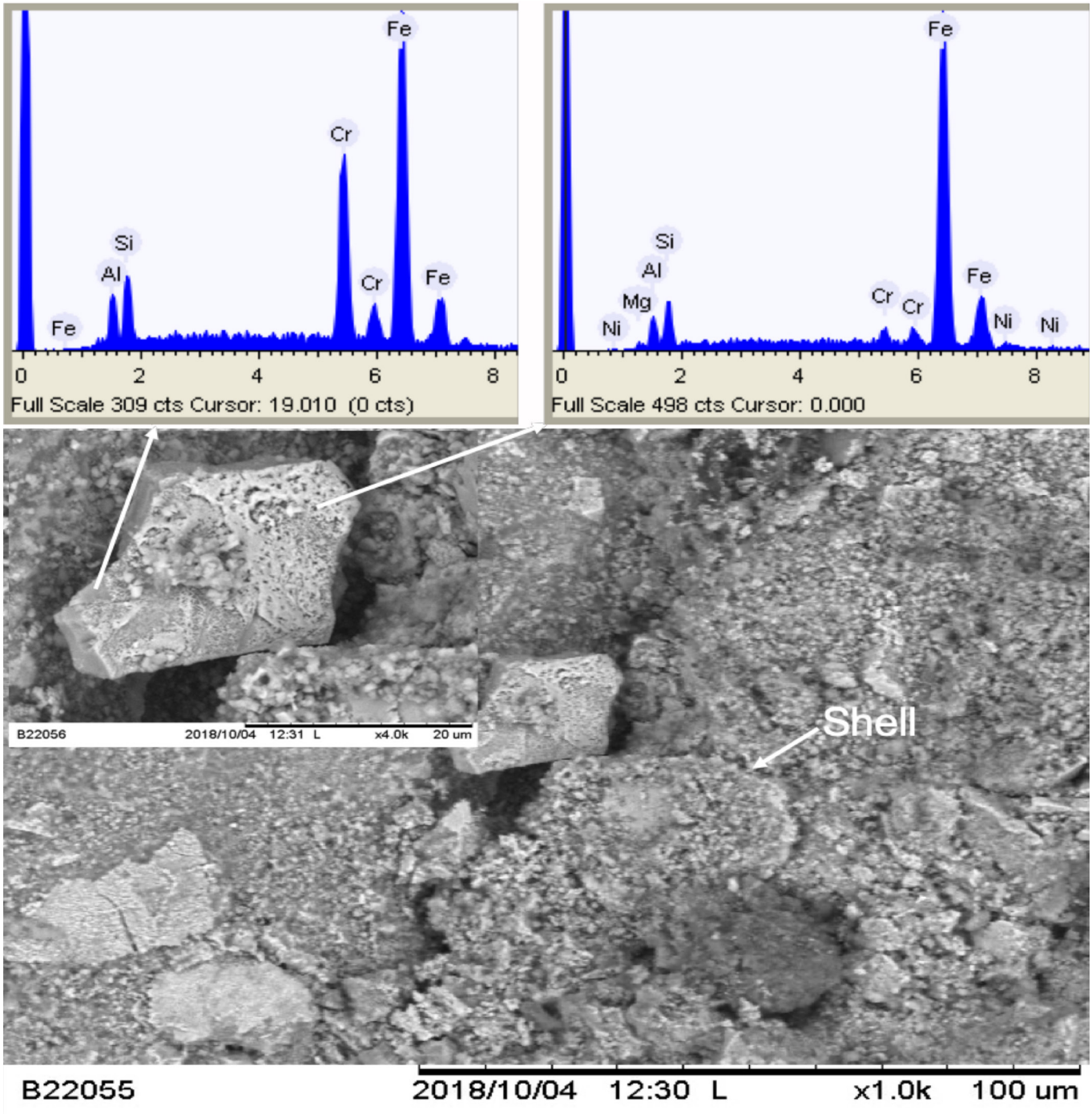

Fig 11 - Black mudstone II facies. Coarse silt size particle of a shell next to Fe-Cr aluminosilicate medium silt size particles. sample_CM19-7A (left). EDX of film covering the Fe-Cr aluminosilicate show by tosudite with Cr, Mn and Ni (1.5 wt %) Sample_CM19-7B (right).

Although common minerals produced by weathering and precipitation of soluble species such as sodium, potassium, calcium, and magnesium can accumulate in sediments as detrital particles, peridotites in this case do not generate detrital particles in the laterite horizons. In contrast, the fine particles seem to evolve in situ as authigenic precipitates on the surfaces of microbial cells (Ferris et al., 1987; Konhauser et al., 1994a; 1994b).

The widespread occurrence of microorganisms in hydrothermal systems contributes to the immobilization of metals through a continuum of sorption and authigenic mineral precipitation reactions (Ferris, 2000). Depending on the prevailing environmental conditions and activity of microbial populations, individual cells can facilitate the nucleation and growth of distinct mineral phases. These processes contribute collectively to the solid phase enrichment of metals in sediments and are presumed to have been instrumental in the formation of some strata-bound ore deposits which are formed under reducing conditions, similar to those proposed for the mudstone succession overlaying the Cerro Matoso peridotites at Pit-1.

In some of the particles, Si/Al ratio varied within a range of approximately 1-4, a silica distribution that is quite similar for consortia of enriched cell cultures indicating active

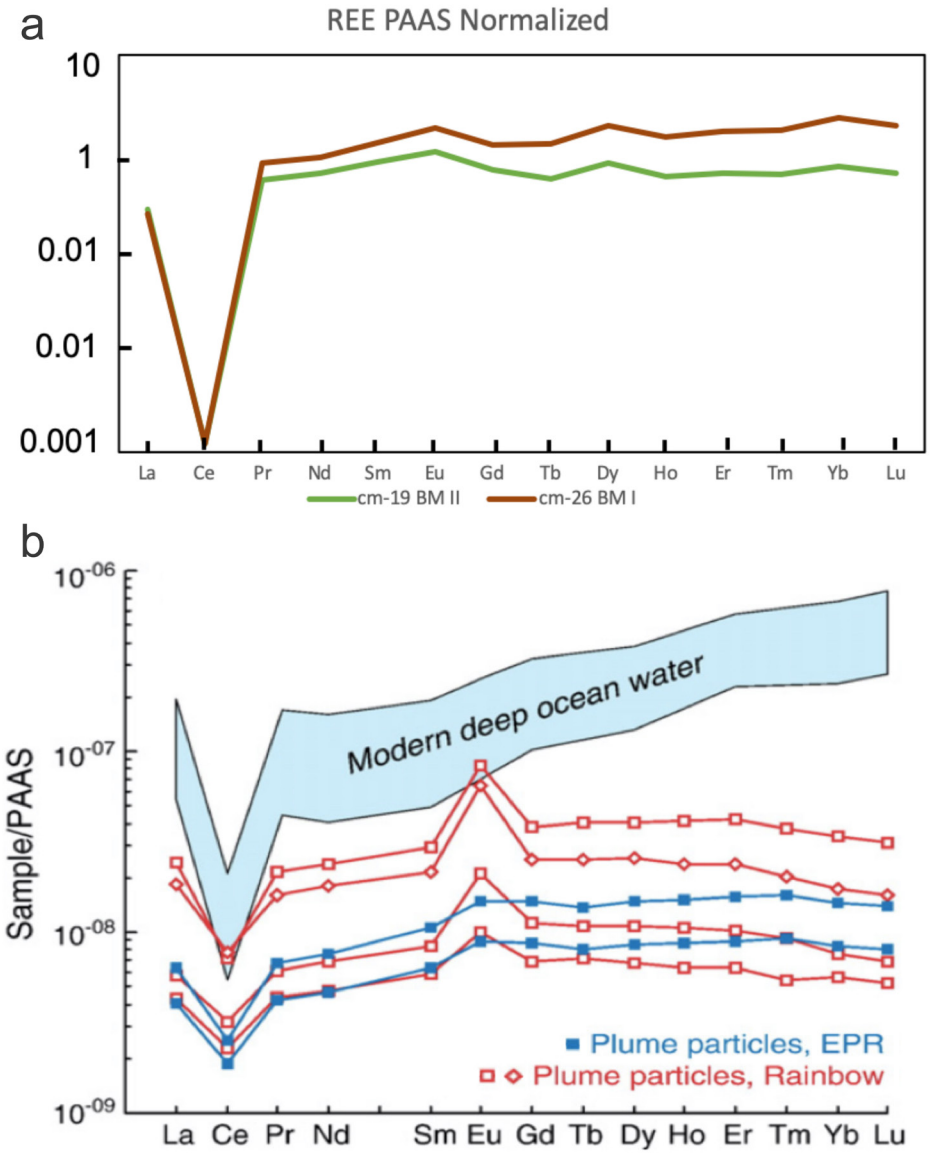

Fig. 12 - a) PAAS normalized REE patterns of Cerro Matoso sediments: Black mudstone facies I and II (BM I and BM II). b) Modern deep ocean water (Byrne and Sholkovitz, 1996), and hydrothermal plume particles from the Rainbow vent field of the Mid- Atlantic Ridge (Edmonds et al., 2004) and the East Pacific Rise at 9°45′N (Sherrell et al., 1999). PAAS data from McLennan et al. (1989) and C, D, after Slack et al. (2007).

silicon mineralization (Chen et al., 2014). The siliceous structure may provide a surface for additional microbial adhesive growth, which is one of the most important survival strategies used by all microorganisms (Dunne, 2002). In the case of aggregates, silicon also could work as cementing material.

Overall, active hydrothermal structures contain TOC concentrations ranging from 0.02 to 1.0 wt% (Kato et al., 2010; Jaeschke et al., 2014; Reeves et al., 2014), and the TOC contents of 0.03-0.1 wt% for BM-I and BM II facies are comparable to those of active chimneys implying high microbial biomass and active microbial activity within the deep marine sediments. Even some of the particles look like organic rests of marine organisms.

The organic aggregates described here could be examples of absorption of metals promoted on the surface of microbial cells in chemically reactive places (i.e., hydrothermal systems), where the mechanisms of microbial mineral precipitation are usually by nucleation and crystal growth favoured by the impact of dissimilatory iron-reducing bacteria on metal cycling in sediments (Gadd, 2010). We suggest that Ni could be incorporated during the formation of solid organics, because during hydrothermal alteration at T < 150ºC abundant Fe-rich phases tend to predominate resulting from significant Fe mobilization /re-deposition and small quantities of Si in these environments reduce the contributions or formation of Fe-rich phyllosilicates (e.g., Suttle et al., 2022) which form the organic envelops. At temperatures > 150ºC the expected Ni-enrichment would be associated with Ni-sulfides which are absent in the investigated samples. However, the hydrothermal experiments of Vinogradoff et al. (2020), carried at 150°C and alkaline pH, demonstrate that the nature of phyllosilicates influences the reaction pathways of organic compounds during hydrothermal alteration, so hydrothermal activity surely does impact the ultimate mineral association of organic aggregates and contribute to sustain the microbial communities.

Oschmann (2000) and Zhang et al. (2001) argued that thermophilic bacteria (T > 45°C) could participate in the reduction of Fe (III) and Mn (IV) during reactions that are important for the immobilization of dissolved metallic elements in sedimentary environments. The mineral immobilization by reducing microbial precipitation may explain part of the mineralization in Cerro Matoso (e.g., manganese, siderite). This type of mineralization has been reported for uranium, copper, bismuth, cobalt accumulates on the outer surfaces of microbial

cells (Milodowski et al., 1990). Of the various microorganisms active in anaerobic sediments, dissimilatory iron and manganese reducers are particularly notable as agents of diagenetic transformations involving metals (Lovley, 1991; Nealson and Saffarini, 1994). The hydrous iron and manganese oxides utilized by these microorganisms occur as discrete particles or as coatings on clay minerals, carbonates, and other particulate material (e.g., microbial cells) that may serve as heterogeneous nucleation sites for oxide deposition (Fortin et al., 1993) and could correspond with the organic aggregates forming the BM I and BM II facies.

The high affinity for the chemical fixation of microbial cells which exhibit dissolved metal ions because of their unique structure and macromolecular composition (Ferris, 2000) may explain the chemical components of the organic aggregates in the marine sediments of Cerro Matoso (i.e., BM I and BM II facies). In this regard, we suggest that extracellular structures forming the aggregate envelopes have strongly enhanced biomineralization mediated by AOM consortia as noted by Chen et al. (2014).

The high Ni content in the studied samples could be related to the biogenic cell-mineral aggregates (CMAs) formed by Fe (II)-oxidizing bacteria and composed of extracellular organic compounds, microbial cells, and ferric iron minerals, which are capable of immobilizing large quantities of nickel via sorption processes (Schmid et al., 2016), especially in systems characterized by elevated concentrations of dissolved metals, such as vent plume sediments. Schmid et al. (2016) indicate that nickel is sorbed by biogenically precipitated iron minerals such as Fe (III)-(oxyhydr)oxides and, to a lesser extent, may be associated with organic compounds. In this case, the nickel must be incorporated during the formation of the aggregates instead of be a product of hydrothermal fluids alteration. Furthermore, the methanogenesis process may be related to a nickel protein (Ni-protein I) which, according to Krüger et al. (2003) and Mayr et al. (2008), may play a catalytic role in AOM and is similar to the nickel cofactor F430 of methyl coenzyme M reductase (MCR), the terminal enzyme of methanogenesis.

The ^{13}C isotope signature (i.e. depleted $\delta^{13}C$ values between -21.6 and -8.1‰ V-PDB, in bulk samples) found in the siderite forming the BM I and BM II facies fit with $\delta^{13}C$ signature of methane-producing microorganisms such as methanogens (Reeburgh, 2007). These latter, in fact, produce methane enriched in ^{13}C yielding isotopic signatures heavier than -25‰. In contrast, values below -25 ‰, which is the average $\delta^{13}C$ in marine organic matter, are associated to anaerobic methane-oxidizing Archaea metabolism (Valentine, 2011) that, together with sulfate-reducing bacteria, participate in the anaerobic methane oxidation (AOM) process (Orphan et al., 2001). In the latter, the responsible for the oxidation of methane, strongly excluding ^{13}C, is the methane monooxygenase.

The shell, circular and ovoid shapes, along with the chemical composition of the organic particles described here, may correspond to anaerobic microorganism consortia fossils whose presence including autotrophic organisms has been also obtained from some subsurface environments including water-flooded oil fields, deep sandy aquifers, deep sediments, granitic groundwater at depths of 10 to 2000 m below sea level and deep-sea hydrothermal vents (Kotelnikova, 2002). This latter was recently identified as a fossilized hydrothermal system hosted by the Cerro Matoso peridotite formed before the Cretaceous age when the set of rocks was accreted to the South America Plate (Castrillón, 2019).

Implications for the Cerro Matoso Ni grades

Initially, the extraordinarily high nickel grades reported at Pit-1 (i.e. > 8 wt%) that distinguishes the Cerro Matoso laterite deposit from other Caribbean Ni-laterites were associated with different or superimposed supergene events (López-Rendón, 1986; Gleeson et al., 2004). The high nickel grade in Cerro Matoso could be also associated with a sulfur-rich hydrothermal vent environment favouring an additional concentration of the high chalcophile nickel (Wedepohl, 1978) in minerals such as millerite (NiS) or eventually pentlandite. In this sense, Vasconcelos and Sebeer, (2006) reported sulfides (pyrite) and sulfates in the ¨black saprolite¨ at Pit-1. Ortiz (2004) reports Cu, Zn, and Ni sulfides in the ¨canga¨ and ¨black saprolite¨ horizons. Both horizons were recently redefined as deep marine sediments (Castrillón, 2019). Although significant amounts of sulfur are necessary to sustain vent communities that get their energy from AOM processes, our analyses point out that the high nickel grades are in the organic aggregates forming the black mudstones I and II facies (i.e., Ni > 4.6 wt%). The evidence presented here suggests biomineralization inducing a Ni-ore favored by reducing conditions and alkaline settings, commonly supported by AOM bacterial cultures associated to hydrothermal systems. This reducing environment favoured the incorporation of nickel into the nimite crystals, as part of the clayish matrix, in the berthierine particles, and in the organic aggregates, contributing to enrich the nickel grades of mudstones and, subsequently, of the laterite deposit.

Using a mass balance model, Gleeson et al. (2004) found Ni enrichment relative to the protolith compared with the change in bulk density of the various units (e.g., ¨black saprolite¨. red laterite, etc.) in Pit-1 and Pit-2, implying that simple Ni upgrading by residual enrichment was not the only process for Ni enrichment in each pit. They suggest a collapse of the laterite profiles, possibly up to 90% of the original volume for Pit-1, and/or supergene mobility of Ni to explain the final Ni grades for Pit-1. The new evidences suggest that hydrothermal Fe-rich sediments with nickel in the different mineral assemblages (e.g., nimite, berthierine, organics) were covering the peridotites and were due to the supergene mobility of Ni. Such inference is supported by the presence of significant Ni concentrations (0.28 ppm) in some of the mine waters (Gleeson et al., 2004). Ni must have been leached from the mudstone horizons before being fixed in the silicates forming green saprolite horizons. Although Ni grades in whole-rock for the "black saprolite", defined here as black mudstones, reaches 1.9 wt% (Gleeson et al., 2004,), our analyses reveal that different hydrothermal minerals contribute to their Ni content.

Once the ultramafic rocks and overlying sediments were accreted to the continent during the Cretaceous (e.g., López-Rendón, 1986; Gleeson et al., 2004; Tobón et al., 2020) and exhumed finally during the Late Miocene (Castrillón et al., 2022) to be exposed to tropical weathering conditions, a supergene nickel enrichment began with saprolitization of the peridotites (i.e., from the clark content of 0.3-0.4 wt% Ni in the forsteritic olivine). During the formation of the laterite profile, nickel was leached from the upper horizons of peridotites and, at the same time, from the Fe-rich mudstones of marine origin that contain organic aggregates with Ni (i.e., BM I and BM II facies). Nickel precipitated mainly as hydrous Ni-Mg silicates in the low-magnesium green saprolite increasing the Ni concentration up to 8 wt% during the rock weathering, forming minerals like pimelite, sepiolite, garnierite and saponite. This is a still active process, as indicated by high Ni-contents in groundwater (Gleeson et al., 2004). An erratic Ni mineralization that

at Pit-1 reaches 9 wt%, corresponds with the Ni-ore known as garnierite veins, clearly seen as veins in the saprolitized peridotites; part of this Ni may come from black horizon leaching. Castrillón and Guerrero (2020) suggest that listvenites with Ni grades reaching 6 wt% underlying the black Fe-rich horizons, contribute to the extraordinary high nickel grades at Cerro Matoso and indicate a hydrothermal influence in the deposit.

Only the combination of these geological processes of primary and secondary enrichment associated with deep-sea hydrothermal and biological processes, plus supergene enrichments allow to explain the differences between Cerro Matoso deposit with other nickel laterites in the Caribbean. Further studies in Cerro Matoso should examine more detailed evidence and effects of these hydrothermal processes and thus possibly yield additional hints for new exploration tools in the numerous ultramafic rock bodies in Colombia and elsewhere.

CONCLUSIONS

The Cerro Matoso peridotites hosted a hydrothermal vent system that permitted the accumulation of black mudstone locally at Pit-1. We propose that these marine sediments contain fossil evidence of organic aggregates formed by methanogen/AOM consortia. The supergene Ni-enrichment of the ultramafic rocks at Cerro Matoso generated Fe-(oxy) hydroxides, pimelite and sepiolite as the major nickel-bearing silicate phases, followed by smectites (saponite), and Ni-silicates (i.e., garnierite) during the different stages of the laterite profile formation.

Ni from the organic aggregates, authigenic clays and silicates forming the mudstone facies (e.g., nimite) plus the hydrothermal nickel enrichment of listvenites contributed to increasing the Ni-grades in the Cerro Matoso during the supergene process.

ACKNOWLEDGEMENTS

The paper presents part of the results of the Ph.D. thesis of the first author (A. Castrillón) who acknowledges a scholarship grant 647 from Colciencias. The authors wish to thank Dr. Fernando Nuñez-Useche, Dr. Teresa Pi Puig and Dr. Augusto Rodriguez from Universidad Nacional Autónoma de Mexico, Instituto de Geología and Instituto de Geofísica Ambiental, and the CONACYT National Laboratories project for their support to LANGEM, and their great support in the thesis end. Our sincere thanks to the reviewers for their constructive comments. Many samples were collected during mine development and fieldwork of AC for Cerro Matoso S.A.

REFERENCES

Alain K., Holler T., Musat F., Elvert M., Treude T. and Krüger M,. 2006. Microbiological investigation of methane- and hydrocarbon-discharging mud volcanoes in the Carpathian Mountains, Romania. Environ. Microbiol., 8: 574-590. https://doi.org/10.1111/j.1462-2920.2005.00922.x

Álvarez J., 1983. Geología de la Cordillera Central y el Occidente Colombiano y petroquímica de los intrusivos granitoides mesocenozoicos. Boletín Geol., 26 (2): 1-175.

Amend J.P., McCollom T.M., Hentscher M. and Bach W., 2011. Catabolic and anabolic energy for chemolithoautotrophs in deep-sea hydrothermal systems hosted in different rock types. Geochim. Cosmochim Acta., 75: 5736-5748.

Andreani M., Escartin J., Delacour A., Ildefonse B., Godard M., Dyment J., Fallick A.E. and Fouquet Y. 2014. Tectonic structure, lithology, and hydrothermal signature of the Rainbow massif (Mid-Atlantic Ridge 36°14'N). Geochem. Geophys. Geosystems., 15: 3543–3571. https://doi:10.1002/ 2014GC005269.

Baker E.T., Lavelle J.W. and Massoth G.J., 1985. Hydrothermal particle plumes over the southern Juan de Fuca Ridge. Nature, 316: 342-344.

Banerji P.K., 1982. Lateritization processes; challenges and opportunities. Episodes, 3: 16-20.

Bardossy G., 1989. Lateritic bauxite deposits; a world-wide survey of observesd facts. Travaux du Comite International pour l´Etude des Bauxites, de l´Alumine, et de l´Aluminium, 19 (22): 11-18.

Bardossy G. and Aleva G.J.J., 1990. Lateritic bauxites. Develop. Econ. Geol., Elsevier, Amsterdam, 27, 624 pp.

Bartok P.E., Renz O., and Westermann D.G.E.G., 1985. The Siquisique ophiolites, northern Lara State, Venezuela: a discussion of their Middle Jurassic ammonites and tectonic implications. Bull. Geol. Soc. Am, 96:1050-1055.

Bau M. and Dulski P., 1999. Comparing yttrium and rare earths in hydrothermal fluids from the Mid-Atlantic Ridge: implications for Y and REE behavior during near-vent mixing and for the Y/Ho ratio of Proteozoic seawater. Chem. Geol., 155: 77-90. https://doi.org/10.1016/S0009-2541(98)00142-9

Bellizia A. and Dengo G., 1990. The Caribbean mountain system, northern South America; a summary. In: G. Dengo and J.E. Case (Eds.), The geology of North America, Vol. H, The Caribbean Region. Geol. Soc. Am., 167-175.

Berger V.I., Singer D.A., Bliss J.D., and Moring B.C., 2011. Ni-Co laterite deposits of the world; database and grade and tonnage models.US Geol. Survey Open-File Rep, 1058: 1-26.

Beukes N., and Klein C., 1990. Geochemistry and sedimentology of a facies transition from microbanded to granular iron formation in the early Proterozoic Transvaal Supergroup, South Africa. Precamb. Res., 47 (1-2): 99-139.

Boetius A., Ravenschlag K., Scubert C.J., Rickert D., Widdel F., Gieseke A., Amann R., Jorgensen B.B., Witte U. and Pfannkuche O., 2000. A marine microbial consortium apparently mediating anaerobic oxidation of methane. Nature, 407: 623-626.

Boström K. and Peterson M., 1969. The origin of aluminium-poor ferromanganoan sediments in areas of high heat flow on the East Pacific Rise. Mar. Geol., 7: 427-447.

Byrne R.H. and Sholkovitz E.R., 1996. Marine chemistry and geochemistry of the lanthanides. Handbook on the physics and chemistry of Rare Earths, 23, 497-593.

Campbell K.A., 2006. Hydrocarbon seep and hydrothermal vent paleoenvironments and paleontology: Past developments and future research directions. Palaeo. Palaeo. Palaeo., 232: 362-407. https//doi:10.1016/j.palaeo.2005.06.018

Cann J.R., Blackman D.K., Smith D.K., McAllister E., Janssen B., Mello S., Avgerinos E., Pascoe A.R. and Escartin J., 1997. Corrugated slip surfaces formed at ridge-transform intersections on the Mid-Atlantic Ridge. Nature, 385: 329-332. https://doi.org/10.1038/385329a0

Cannat M., Sauter D., Mendel V., Ruellan E., Okino K., Escartin J., Combier V. and Baala M., 2006. Modes of seafloor generation at a melt-poor ultraslow-spreading ridge. Geology, 34: 605-608. https://doi.org/10.1130/G22486.1.

Cardona A., Weber M., Wilson R., Cordani U., Muñoz C.M. and Paniagua F., 2007. Evolución tectono-magmática de las rocas máficas-ultramáficas del Cabo de La Vela y el Stock de Parashi, Peninsula de la Guajira: registro de la evolución orogénica Cretácica-Eocena del norte de Suramerica y el Caribe. "XI Congreso Colombiano de Geología". Bucaramanga, 14-17.

Castrillón A., 2019. Carbonatos y otros minerales autigénicos asociados a las lateritas niquelíferas de Cerro Matoso y su posible relación con actividad hidrotermal y reducción de sulfatos. Univ. Nacion. de Colombia. PhD Thesis. 209 pp.

Castrillón A. and Guerrero J., 2020. Listvenites: new insights of a hydrothermal system fossilized in Cerro Matoso peridotites, Montelíbano, Córdoba Department, Colombia. Bol. Geol., 47: 67-84. https://doi.org/10.32685/0120-1425/boletingeo.47.2020.492

Castrillón A., Pi-Puig T., Guerrero J., Nuñez-Useche F., Rodriguez A. and Canet C., 2022. Clay mineralogy and texture of deep-sea hydrothermal mudstone associated with the Cerro Matoso peridotite in accreted oceanic crust from Colombia. J. South Am. Earth Sci. 117: 1-16. https://doi.org/10.1016/j.jsames.2022.103886

Cediel F., Shaw R.P. and Cáceres C., 2003. Tectonic assembly of the Northern Andean Block. The Circum-Gulf of Mexico and the Caribbean: Hydrocarbon habitats, basin formation and plate tectonics. AAPG Mem., 79: 815-848.

Charlou J.L., Donval J.P., Fouquet Y., Jean-Baptiste P. and Holm N., 2002. Geochemistry of high H_2 and CH_4 vent fluids issuing from ultramafic rocks at the Rainbow hydrothermal field (36°14′N, MAR) Chem. Geol., 191 (4): 345-359.

Chavagnac V., German C., Milton J. and Palmer M., 2005. Source of REE in sediment cores from the Rainbow vent site (36º14′N, MAR). Chem. Geol., 216: 329-352.

Chen Y., Li Y-L., Zhou G-T., Li H., Lin Y-T., Xiao X. and and Wang F-P., 2014. Biomineralization mediated by anaerobic methane-consuming cell consortia. Sci. Rep., 4 (5696). DOI:10.1038/srep05696.

Chicangana G., Kammer A., Vargas C.A., Ordóñez C.I., Mora H., Ferrari A.L. and López S.A., 2011. El posible origen de la sismicidad somera que se presenta en la region que corresponde a la Sierra Nevada de Santa Marta, la Serranía de Perijá y la Península de la Guajira, noreste de Colombia. Dialnet Cap and Cua., 6 (1): 1-33.

Dilek Y., 2003. Ophiolite pulses, mantle plumes and orogeny. Geol. Soc. London Spec. Publ., 218: 9-19. https://doi.org/10.1144/GSL.SP.2003.218.01.02

Douville E., Charlou J.L., Oelkers E.H., Bienvenu P., Jove Colon C.F., Danval J.P., Fouquet Y., Prieur D., and Appriou P., 2002. The rainbow vent fluids (36°14′N, MAR): the influence of ultramafic rocks and phase separation on trace metal content in Mid-Atlantic Ridge hydrothermal fluids. Chem. Geol., 184: 37-48.

Dueñas H. and Duque H., 1981. Geología del Cuadrángulo F-8. Bol. Geol., 24 (1): 1-35.

Dunne W.M., 2002. Bacterial adhesion: seen any good biofilms lately? Clin. Microbiol. Rev., 15: 155-166. https://dx.doi.org/10.1128%2FCMR.15.2.155-166.2002

Edmonds H.N. and German C.R., 2004. Particle geochemistry in the Rainbow hydrothermal plume, Mid-Atlantic Ridge. Geochim. Cosmochim. Acta, 68: 759-772.

Ehrlich H., Demadis K.D., Pokrovsky O.S. and Koutsoukos P.G., 2010. Modern views on desilicification: biosilica and abiotic silica dissolution in natural and artificial environments. Chem. Rev. 110: 4656-4689. https://doi.org/10.1021/cr900334y

Eickmannn B., Bach W. and Peckmann J., 2009a. Authigenesis of carbonate minerals in modern and Devonian ocean floor hard rocks. J. Geol., 117 (3): 307-323.

Eickmann B., Bach W., Rosner M. and Peckmann J. 2009b. Geochemical constraints on the modes of carbonate precipitation in peridotites from Logatchev Hydrothermal Vent Field and Gakkel Ridge. Chem. Geol., 268 (1-2): 97-106. https://doi.org/10.1016/j.chemgeo.2009.08.002

Escartin J., Mével C., MacLeod C.J. and McCaig A.M., 2003. Constraints on deformation conditions and the origin of oceanic detachments: The Mid-Atlantic Ridge core complex at 15°45'N. Geochem, Geophys, Geosyst., 4: 1-37. https://doi:10.1029/2002GC000472

Feely R.A., Lewison M., Massoth G.J., Robert-Baldo G., Lavelle W., Byrne R.H., von Damm K.V. and Curl Jr H.C., 1987. Composition and dissolution of black smoker particles from active vents on the Juan de Fuca Ridge. J. Geophys. Res., 92 (B11): 347-363.

Ferris FG., 2000. Microbe-metal interactions in sediments. In: R.E. Riding and S.M. Awramik (Eds.). Microbial sediments, 121-126. Springer, Berlin, Heidelberg.

Ferris FG., Beveridge T. and Fyfe W., 1986. Iron-silica crystallite nucleation by bacteria in a geothermal sediment. Nature, 320: 609-611.

Ferris FG., Fyfe W.S., and Beveridge T.J., 1987. Bacterial as nucleation sites for authigenic minerals in a metal-contaminated lake sediment. Chem. Geol., 63:225-232

Friedrich G., Marker A., Kanig M. and Germann A., 1987. Mineral prospecting and geological mapping in laterite covered areas of Brazil. BMFT RG 83015 Final Report, lnstitut ffir Mineralogie,RWTH Aachen, 375 pp.

Fortin D., Leppard G.G. and Tessier A., 1993. Characteristics of lacustrine diagenetic iron oxyhydroxides. Geochim. Cosmochim Acta., 57: 4391-4404

Frost R.B., and Beard J.S., 2007. On silica activity and serpentinization. J. Petrol., 48: 1351-1368. https://doi.org/10.1093/petrology/egm021

Furnes H., Muehlenbachs K., Torsvik T., Thorseth I.H. and Tumyr O., 2001. Microbial fractionation of carbon isotopes in altered basaltic glass from the Atlantic Ocean, Lau Basin and Costa Rica Rift. Chem. Geol., 173: 313-330. https://doi.org/10.1016/S0009-2541(00)00285-0

Gadd G.M., 2010. Metals, minerals and microbes: geomicrobiology and bioremediation. Microbiol., 156: 609-643, https://doi.org/10.1099/mic.0.037143-0

German C.R., Higgs NC.J., Thomson R., Mills H., Elderfield J., Blusvtajn A.P., Flee and Bacon M.P., 1993. A geochemical study of metalliferous sediment from the TAG hydrothermal mound, 26°08'N, MAR. J. Geophys. Res., 98: 9683-9692.

Gleeson S.A., Herrington R.L., Durango J. and Velazquez C.A., 2004. The mineralogy and geochemistry of the Cerro Matoso S.A Ni Laterite Deposit, Montelibano, Córdoba. Econ. Geol., 99: 1197-1213. https://doi.org/10.2113/gsecongeo.99.6.1197.

Grossman E.L., Cifuentes L.A. and Cozzarelli I.M., 2002. Anaerobic methane oxidation in a landfill-leachate plume. Environ. Sci. Technol., 36: 2436-2442. https://doi.org/10.1021/es015695y.

Han X., Suess E., Sahling H. and Wallman K., 2004. Fluid venting activity on the Costa Rica margin: new results from authigenic carbonates. Intern. J. Earth Sci., 93: 596-611.

Hein J.R., Koschinsky A., Halbach P., Manheim F.T., Bau M., Kang J.K. and Lubick N., 1997. Iron and manganese oxide mineralization in the Pacific. In: K. Nicholson, J.R. Hein, B. Bu«hn and S. Dasgupta (Eds.), Manganese mineralization: geochemistry and mineralogy of terrestrial and marine deposits. Geol. Soc. London Spec. Publ., 119: 123-138.

Hentscher M., 2012. Thermodynamic investigations of microbial metabolism and abiotic organic synthesis in seafloor hydrothermal systems. Doctoral dissertation, Universität Bremen, 103 pp.

Hodel F., Macouin M., Trindade R.I.F., Triantafyllou A., Ganne J., Chavagnac V., Berge, J., Rospabé M., Destrigneville C., Carlut J., Ennih N. and Agrinier P., 2018. Fossil black smoker yields oxygen isotopic composition of Neoproterozoic seawater. Nature Comm., 9: 1453, https://doi.org/10.1038/s41467-018-03890-w.

Hongo Y., Obata H., Gamo T., Nakaseama M., Ishibashi J., Konno U., Saegusa S., Ohkubo S. and Tsunogai U., 2007. Rare Earth Elements in the hydrothermal system at Okinawa Trough back-arc basin. Geochem. J., 41: 1-15. https://doi.org/10.2343/geochemj.41.

Hoyos N. and Velázquez C.A., 1996. Análisis del origen de la lateritización y saprolitización del yacimiento niquelífero de Cerro Matoso: Medellín, Colombia, Univ. EAFIT, MSci. Thesis, 99 pp.

Ildefonse B., Rona P.A. and Blackman D., 2007. Drilling the crust at Mid-Ocean Ridge. An in depth perpective. Oceanography, 20 (1): 66-77.

Jaeschke A., Jorgensen S.L., Bernasconi S.M. and Pedersen R.B., 2012. Microbial diversity of Loki's Castle black smokers at the Arctic Mid-Ocean Ridge. Geobiol., 10: 548-561. https://doi.org/10.1111/gbi.12009.

Jaeschke A., Eickmann B., Lang S.Q., Bernasconi S.M., Strauss H., and Fruhe-Green G.L., 2014. Biosignatures in chimney structures and sediments from the Loki's Castle low-temperature hydrothermal vent field at the Arctic Mid-Ocean Ridge. Extremophiles 18, 545–560. doi: 10.1007/s00792-014-0640-2

Johnson C., Beard B., Beukes N., Klein C. and O`Leary J., 2003. Ancient geochemical cycling in the Earth as inferred from Fe isotope studies of banded iron formations from the Transvaal Craton. Contrib. Miner. Petrol., 144: 523-547.

Kappler A., Pasquero C., Konhauser K.O. and Newman D.K., 2005. Deposition of banded iron formations by anoxygenic phototrophic Fe(II)-oxidizing bacteria. Geology, 33: 865-868. https://doi.org/10.1130/G21658.1

Kato S., Takano Y., Kakegawa T., Oba H., Inoue K., Kobayashi C. et al. 2010. Biogeography and biodiversity in sulfide structure of active and inactive vents at deep-sea hydrothermal fields of the Southern Mariana Trough. Appl. Environ. Microbiol., 76: 2968-2979. https://doi.org/10.1128/AEM.00478-10.

Kelley D. and Shank T., 2010. Hydrothermal systems: A decade of discovery in slow spreading environments. Geophys. Monogr. Series, 188: 369-407.

Kerr A.C., Marriner G.F., Tarney J., Nivia A., Saunders A.D., Thirlwall M.F. and Sinton C.W., 1997. Cretaceous basaltic terranes in western Colombia: Elemental, chronological and Sr-Nd isotopic constraints on petrogenesis: J. Petrol., 38: 677-702. https:// doi.org/10.1093/petroj/38.6.677

Knittel K. and Boetius A., 2009. Anaerobic oxidation of methane: progress with an unknown process. Ann. Rev. Microbiol., 63: 311-334. https://doi.org/10.1146/annurev.micro.61.080706.093130

Konhauser K. and Riding R., 2012. Bacterial biomineralization. In: H. Knoll, D. E. Canfield and K. O. Konhauser (Eds.). Fundamentals of Geobiology, A. (Hoboken, New Jersey: John Wiley and Sons), 105-130.

Konhauser K.O. and Urrutia M.M., 1999. Bacterial clay authigenesis: a common biogeochemical process. Chem. Geol., 161: 399-413.

Konhauser KO., Fyfe WS., Schultze Lam S., Ferris FG. and Beveridge TJ., 1994a. Iron phosphate precipitation by epilithic microbial bio- films in Arctic Canada. Can. J. Earth. Sci., 31: 1320-1324.

Konhauser K.O., Hamade T., Raiswell R., Morris R.C., Grant Ferris F., Southam G. and Canfield D.E., 2002. Could bacteria form Precambrian banded iron formations? Geology, 30: 1079-1082. https://doi.org/10.1130/0091-7613(2002)030%3C1079:CBHFTP%3E2.0.CO;2

Konhauser K.O., Schultze Lam S., Ferris F.G., Fyfe W.S., Longstaffe F. and Beveridge J.J., 1994b. Mineral precipitation by epilithic biofilms in the speed river, Ontario, Canada. Appl. Environ. Microbiol., 60: 549-553

Kotelnikova S., 2002. Microbial production and oxidation of methane in deep subsurface. Earth. Sci. Rev., 58: 367-395. https://doi.org/10.1016/S0012-8252(01)00082-4

Krüger M., Meyerdierks A., Glöckner F.O., Amann R., Widdel F., Kube M., Reinhardt R., Kahnt J., Böcher R., Thauer R.K. and Shima S., 2003. A conspicuous nickel protein in microbial mats that oxidize methane anaerobically. Nature. 426: 878-881

Kuhn T., Bau M., Blum N. and Halbach P., 1998. Origin of negative Ce anomalies in mixed hydrothermal–hydrogenetic Fe-Mn crusts from the Central Indian Ridge. Earth Planet. Sci. Lett., 163 (1): 207-220. https://dx.doi.org/10.1016/S0012-821X(98) 00188-5

Lartaud F., de Rafélis M.., Oliver G., Krylova E., Dyment J., Ildefonse B., Thibaud R., Gente P., Hoisé E., Meistertzheim A-L., Fouquet Y., Gaill F. and Le Bris N., 2010. Fossil clams from a serpentinite-hosted sedimented vent field near the active smoker complex Rainbow, MAR, 36 degrees 13´ N: Insight into the biogeography of vent fauna. Geochem. Geophys. Geosyst. 11, Q0AE01. https://doi.org/10.1029/2010GC003079

Laurila T.E., Hannington M.D., Leybourne M., Petersen S., Devey C.W. and Scho∈nberg D.G., 2015. New insights into the mineralogy of the Atlantis II Deep metalliferous sediments, Red Sea. Geochem. Geophys. Geosyst., 16: 4449-4478. https://doi:10.1002/2015GC006010.

Lewis J.F., Draper G., Proenza J.A., Epaillat J. and Jiménez J., 2006. Ophiolite-related ultramafic rocks (serpentinites) in the Caribbean Region: A Review of their ocurrence, composition, origin, emplacement and Ni-laterite soil formation. Geol. Acta, 4 (1-2): 237-263. https://doi.org/10.1344/105.000000368

López-Rendón, J. 1986. Geology, mineralogy and geochemistry of the Cerro Matoso Nicheliferous Laterite, Córdoba, Colombia. Thesis Doctoral.Colorado State University. 378 pp.

Lovley D.R., 1991. Dissimilatory Fe (III) and Mn (IV) reduction. Microbiol. Rev., 55: 259-287.

Marques A.F., Barriga A., Chavagnac F.V. and Fouquet Y., 2006. Mineralogy, geochemistry, and Nd isotope composition of the Rainbow hydrothermal field, Mid-Atlantic Ridge. Miner. Dep. 41: 52-67.

Mayr S., Latkoczy C., Krüger M., Günther D., Shima S., Thauer R.K., Widdel F. and Jaun B., 2008. Structure of an F430 variant from Archaea associated with anaerobic oxidation of methane. J. Am. Chem. Soc, 130 (32), 10758-10767. https://doi.org/10.1021/ja802929z.

McLennan S.M., McCulloch M.T., Taylor S.R. and Maynard, J.B., 1989. Effects of sedimentary sorting on Neodymium isotopes in deep-sea turbidites. Nature, 337: 547-549.

Meissener R.O., Flueh E.R., Stibane F. and Berg E., 1982. Dynamics of active plate boundary in southwestern Colombia according to recent geophysical measurements. Tectonophysics, 35: 115-136.

Mejia V.M. and Durango J.R., 1981. Geologia de las lateritas niquelíferas de Cerro Matoso. Bol. Geol., 15: 117-123.

Ménez B., Pasini V. and Brunelli D., 2012. Life in the hydrated suboceanic mantle. Nat. Geosci., 5: 133-137.

Metz S., Trefry I.H. and Nelsen T., 1988. History and geochemistry of a metalliferous sediment core from the Mid-Atlantic Ridge. Geochim. Cosmochim Acta., 48: 47-62.

Mills R., Elderfield H. and Thomson J., 1993. A dual origin for the hydrothermal component in a metalliferous sediment core from the Mid-Atlantic Ridge. J. Geophys. Res., 98: 9671-9681.

Milodowski A.E., West JM., Pearce J.M., Hyslop E.K., Basham I.R. and Hooker P.J., 1990. Uranium-mineralized microorganisms associated with uraniferous hydrocarbons in southwest Scotland. Nature., 347: 465-467.

Mora J.A., Oncken O., Le Breton E., Ibánez-Mejia M., Faccenna C., Veloza G., Velez V., de Freitas M. and Mesa A., 2017. Linking Late Cretaceous to Eocene tectonostratigraphy of the San Jacinto Fold Belt of NW Colombia with Caribbean Plateau collision and flat subduction. Tectonics, 36 (11): 2599-2629.

Naciones Unidas, 1975. Evaluación de lateritas niquelíferas en los Departamentos de Córdoba y Antioquia: Nueva York, informe técnico para el Gobierno de Colombia, 286 pp.

Nan J., King H.E., Delen F., Meirer F., Weckhuysen B.M., Guo Z., Peng X. and Plümper O., 2021. The nanogeochemistry of abiotic carbonaceous matter in serpentinites from the Yap Trench, western Pacific Ocean: Geology, 49: 330-334. https://doi.org/10.1130/G48153.1

Nauhaus K., Albrecht M., Elvert M., Boetius A. and Widdel F., 2007. In vitro cell growth of marine archaeal-bacterial consortia during anaerobic oxidation of methanewith sulfate. Environ Microbiol., 9: 187-196. https://doi.org/10.1111/j.1462-2920.2006.01127.x

Nealson K.H. and Saffarini D., 1994. Iron and manganese in anaerobic respiration: Environmental significance, physiology, and regulation. Ann. Rev. Microbiol., 48: 311-343.

Nívia A., 1997. El Complejo Estructual Dagua, Registro de Deformación de la Provincia Litosférica Oceánica Cretácica Occidental en un Prisma Acrecionario. VII Congreso Colombiano de Geología, Tomo III, 54-67.

Nivia A., 1996. The Bolivar mafic-ultramafic complex, SW Colombia: the base of an obducted oceanic plateau: J. South Am. Earth Sci., 9: 59-68. https://doi.org/10.1016/0895-9811(96)00027-2

Orcutt B.N., Bradley J., Brazelton W.J., Estes E.R., Goordial J.M., Huber J.A., Jones R.M., Mahmoudi N., Marlow J.J., Murdock S. and Pachiadaki M., 2018. Impacts of deep-sea mining on microbial ecosystem services. Limn. Ocean., 65 (7): 1489-1510. https://doi.org/10.1002/lno.11403

Orphan V.J., Hinrich K-U., Ussler III W., Paul C.K., Taylor L.T., Sylva S.P., Hayes J.M. and Delong E.F., 2001. Comparative analysis of methane-oxidizing archaea and sulfate-reducing bacteria in anoxic marine sediments. Appl. Environ. Microbiol., 67(4): 1922-1934. https://doi.org/10.1128/AEM.67.4.1922-1934.2001

Ortiz F., 2004. Guías para la localización de metales preciosos en ofiolitas colombianas. Ofiolitas: Características mineralógicas y petrográficas del yacimiento de níquel de Cerro Matoso. DYNA, 71 (142): 11-23.

Oschmann W., 2000. Microbes and Black Shales. In: R.E. Riding and S.M. Awramik (Eds.), Microbial Sediments. 331 pp.

Pasini V., Brunelli D., Dumas P., Sandt C., Frederick J., Benzerara K., Bernard S. and Ménez B., 2013. Low temperature hydrothermal oil and associated biological precursors in serpentinites from mid-ocean ridge. Lithos., 178: 84-95. https://doi.org/10.1016/j.lithos.2013.06.014

Paulick H., Bach W., Godard M., De Hoog J.C.M., Suhr G. and Harvey J., 2006. Geochemistry of abyssal peridotites (Mid-Atlantic Ridge, 15°20′N, ODP Leg 209): Implications for fluid/rock interaction in slow spreading environments. Chem. Geol., 234: 179-210. https://doi.org/10.1016/j.chemgeo.2006.04.011

Perner M., Bach W., Hentscher M., Koschinsky A., Garbe-Schönberg D., Streit W.R. and Strauss H., 2009. Short-term microbial and physico-chemical variability in low-temperature hydrothermal fluids near 5°S on the Mid-Atlantic Ridge. Environ. Microbiol., 11: 2526-2541. https://doi.org/10.1111/j.1462-2920.2009.01978.x

Phoenix V.R., and Konhauser K.O., 2008. Benefits of bacterial biomineralization. Geobiol., 6: 303-308. https://doi.org/10.1111/j.1472-4669.2008.00147.x

Pindell J.L. and Barrett S.F., 1990. Geological evolution of the Caribbean region: a plate tectonic perspective. In: J.L Pindell and S.F Barrett (Eds.), The Caribbean Decade of North American Geology, Geol. Society Amer. Vol H, The Caribbean Region p. 405-433. https://doi.org/10.1144/SP328.1

Pindell J.L, and Kennan L., 2009. Tectonic evolution of the Caribbean and northern South America in the mante reference frame: un update. Geol. Soc. London Spec. Publ., 328: 1-55.

Reeburgh W.S., 2007. Oceanic methane biogeochemistry. Chem. Rev, 38: 486-513. https://doi.org/10.1021/cr050362v

Reeves E.P., Yoshinaga M.Y., Pjevac P., Goldenstein N.I., Peplies J., Meyerdierks A., et al., 2014. Microbial lipids reveal carbon assimilation patterns on hydrothermal sulfide chimneys. Environ. Microbiol., 16: 3515-3532. https://doi.org/10.1111/1462-2920.12525

Schmid G., Zeitvogel F., Hao L., Ingino P., Adaktylon I., Eickhoff M. and Obst M., 2016. Submicron-scale heterogeneities in nickel sorption of various cell-mineral aggregates formed by Fe(II)-oxidizing bacteria environ. Sci. Technol., 50 (1): 114-12. https://doi.org/10.1021/acs.est.5b02955

Schrenk M., Brazelton W. and Lang S., 2013. Serpentinization, carbon and deep life. Rev. Miner. Geochem, 7: 575-606. https://doi.org/10.2138/rmg.2013.75.18

Schwarz T., 1994. Laterites: concepts, geology, morphology and chemistry. Clay Miner., 31: 440-441.

Sforna M.C., Brunelli D., Pisapia C., Pasini V., Malferrari D. and Ménez B., 2018. Abiotic formation of condensed carbonaceous matter in the hydrating oceanic crust. Nature Commun., 9: 5049. https:/doi.org/10.1038/s41467-018-07385-6

Sherwood L.B., Lacrampe-Couloume G., Slater G.F., Ward J., Moser D.P., Gihring T.M., Lin L.H. and Onstott T.C., 2006. Unravelling abiogenic and biogenic sources of methane in the Earth's deep subsurface. Chem. Geol., 226: 328-339. https://doi.org/10.1016/j.chemgeo.2005.09.027

Sherrell R.M., Field M. P. and Ravizza, G., 1999. Uptake and fractionation of Rare Earth Elements on hydrothermal plume particles at 9 45′N, East Pacific Rise. Geochim. Cosmochim. Acta, 63: 1709-1722.

Silantyev S.A., Mironenko M.V. and Novoselov A.A., 2009. Hydrothermal systems in peridotites of slow-spreading mid-oceanic ridges. Modeling phase transitions and material balance: downwelling limb of a hydrothermal circulation cell. Petrology, 17 (2): 138-157.

Sinton C.W., Duncan R.A., Storey M., Lewis J. and Estrada J.J., 1998. An oceanic flood basalt province within the Caribbean Plate. Earth Planet. Sci. Lett., 155: 221-235.

Slack J.F., Grenne T., Bekker A., Rouxel O.J. and Lindberg P.A., 2007. Suboxic deep seawater in the late Paleoproterozoic: Evidence from hematitic chert and iron formation related to seafloor-hydrothermal sulfide deposits, central Arizona, USA. Earth Planet. Sci. Lett., 255: 243-256. https://doi.org/10.1016/j.epsl.2006.12.018

Smith D.K., Cann J.R. and Escartin J., 2006. Widespread active detachment faulting and core complex formation near 13° N on the Mid-Atlantic Ridge. Nature, 442: 440-443. https://doi.org/10.1038/nature04950.

South32., 2019. Annual Report 2019 (online): Western Australia, available in <south32. net/investors-media/investor-centre/ annual-report-suite>, visited on November 1st, 2019.

Spadea P. and Espinosa A., 1996. Petrology and chemistry of late Cretaceous volcanic rocks from the southernmost segment of the Western Cordillera of Colombia (South America). J. South Am. Earth Sci., 9: 79-90. https://doi.org/10.1016/0895-9811(96)00029-6

Suttle M.D., King A.J., Ramkissoon N.K., Bonato E., Franchi I.A., Malley J., Schofield P.F., Najorka J., Salge T. and Russell S.S., 2022. Alteration conditions on the CM and CV parent bodies. Insights from hydrothermal experiments with the CO chondrite Kainsaz. Geochim. Cosmochim Acta., 318: 83-111. https://doi.org/10.1016/j.gca.2021.11.028

Tobón M., Weber M., Proenza J. A., Aiglsperger T., Betancur S., Farré-de- Pablo J., Ramírez C. and Pujol-Solà N. 2020. Geochemistry of Platinum-Group Elements (PGE) in Cerro Matoso and Planeta Rica Ni-Laterite deposits, Northern Colombia: Bol. Soc, Geol. Mex., 72 (3), A201219. http://dx.doi.org/10.18268/BSGM2020v72n3a201219.

Toner B.M., Santelli C.M., Marcus M.A., Wirth R., Chan C.S., McCollom T., Bach W. and Edwards K.J., 2009. Biogenic iron oxyhydroxide formation at mid-ocean ridge hydro-thermal vents: Juan de Fuca Ridge. Geochim. Cosmochim Acta., 73: 388-403. https://doi.org/10.1016/j.gca.2008.09.035

Tyler P.A. and Young C.M., 2003. Dispersal at hydrothermal vents: a summary of recent progress. Hydrobiology., 503: 9-19.

Valentine D.L., 2011. Emerging topics in marine methane biogeochemistry. Ann. Rev. Mar. Sci., 3: 147-171. https://doi.org/10.1146/annurev-marine-120709-142734

Vasconcelos P. and Seeber A., 2006. UQ Field Trip to Cerro Matoso. Dept. Earth Sci. Univ. Queensl. Initial Rep., 28 pp.

Villagómez D., 2010. Thermochronology, geochronology and geochemistry of the Western and Central Cordilleras and Sierra Nevada de Santa Marta, Colombia: The tectonic evolution of NW South America. PhD. Thesis, Univ. Genève, 142 pp.

Vinogradoff V., Le Guillou C., Bernard S., Viennet J.C., Jaber M. and Remusat L., 2020. Influence of phyllosilicates on the hydrothermal alteration of organic matter in asteroids: Experimental perspectives. Geochim. Cosmochim Acta., 269: 150-166. https://doi.org/10.1016/j.gca.2019.10.029

Wedepohl K.H., 1978. Handbook of Geochemistry, Vol. 3, Berlin: Springer-Verlag. 442 pp.

Whiticar M.J., 1999. Carbon and hydrogen isotope systematics of bacterial formation and oxidation of methane. Chem. Geol., 161: 291-314.

Woese C.R., Kandler O. and Wheelis M.L., 1990. Towards to a natural system of organisms. Proposal for the domains Archaea, Bacteria and Eucaria. Proc. Natl. Acad. Sci. U.S., 87: 44576-44579.

Zhang C., Horita J., Cole D., Zhou J., Lovley D. and Phelps J. 2001. Temperature-dependent oxygen and carbon isotope fractionations of biogenic siderite. Geochim. Cosmochim Acta., 65 (14): 2257-2271. https://doi.org/10.1016/S0016-7037(01)00596-8.

Received, September 6, 2021
Accepted, April 24, 2022